Article:

Frischbutter, AA, Fisher, QJ orcid.org/0000-0002-2881-7018, Namazova, G et al. (1 more author) (2017) The value of fault analysis for field development planning. Petroleum Geoscience, 23 (1). pp. 120-133. ISSN 1354-0793

https://doi.org/10.1144/petgeo2016-053

The value of fault analysis for field development planning

Andreas A. Frischbutter[1]*, Quentin J. Fisher[2], Gyunay Namazova[1] & Sebastien Dufour[1]

[1]Wintershall Norge AS, Laberget 28, 4020 Stavanger, Norway
[2]School of Earth and Environment, University of Leeds, Leeds, LS2 9JT, UK
*Corresponding author (Andreas.Frischbutter@wintershall.com)

Work carried out at **Wintershall Norge AS** and **Center for Integrated Petroleum Geoscience, University of Leeds**

Abbreviated title: Fault analysis in field development planning

Abstract: Faults play an important role in reservoir compartmentalization and can have a significant impact on recoverable volumes. A recent petroleum discovery in the Norwegian offshore sector, with an Upper Jurassic reservoir, is currently in the development planning phase. The reservoir is divided into several compartments by syn-depositional faults that have not been reactivated and do not offset the petroleum-bearing sandstones completely. A comprehensive fault analysis has been conducted from core to seismic scale to assess the likely influence of faults on the production performance and recoverable volumes. The permeability of the small-scale faults from the core were analyzed at high confining pressures using formation compatible brines. These permeability measurements provide important calibration points for the fault property assessment, which was used to calculate transmissibility multipliers (TM) that were incorporated into the dynamic reservoir simulation model to account for the impact of faults on fluid flow. Dynamic simulation results reveal a range of more than 20% for recoverable volumes depending on the fault property case applied and for a base case producer/injector well pattern. The fault properties are one of the key parameters that influence the range of cumulative recoverable oil volumes and the recovery efficiency.

Keywords: fault property analysis, fault permeability prediction, fault rock petrophysics, transmissibility multiplier, dynamic reservoir simulation, field development planning

Introduction

A recently discovered oil field with a gas cap in the Norwegian offshore sector is currently in the development planning phase. Four exploration/appraisal wells have been drilled in the field, but no production data exists at this stage of the field lifecycle. Key uncertainties that impact recoverable volumes and production behaviour range from reservoir distribution (i.e. sedimentologically-controlled compartmentalization), reservoir properties, fault architecture and fault rock properties. In terms of the latter, the field is compartmentalized by numerous faults at the seismic scale, but also contains numerous sub-seismic scale faults. An understanding of the fault properties and their influence on the field production and recoverable volumes is essential for assessing the fields economics, planning a production strategy and also influences the design of the facilities. In this paper we focus on the impact of structural pattern and fault rock properties on the subsurface fluid flow and hence the production.

Workflows exist for the quantitative assessment of the impact of faults on fluid flow in petroleum reservoirs and can be implemented using a range of software tools that are commonly available (see review by Fisher & Jolley, 2007). In general, the workflow begins by undertaking a structural analysis using seismic data. Faults identified from seismic are then incorporated into the geological model. The clay distribution along the faults is then estimated using well established algorithms. In siliciclastic reservoirs, the main fault seal processes are: (i) cataclasis; (ii) mixing of clays with framework grains, (iii) clay smear, and (iv) post-deformation diagenesis such as quartz cementation and grain-contact quartz dissolution (Fisher and Knipe, 1998; 2001). The presence of clay is important for two of these mechanisms which often results in correlations between fault permeability and clay content; these correlations may then be used to calculate transmissibility multipliers (TM) that are incorporated into simulation models to take into account the impact of faults on fluid flow. Fault rock permeability data can be obtained from global datasets. However, some studies suggest that better results are obtained if fault permeability estimates are based on the laboratory measurements made on fault rocks sampled from cores taken within the field being appraised or from nearby analogues (Fisher & Knipe, 2001; Sperrevik et al., 2002; Jolley et al., 2007).

The study reported in this paper follows the general workflow described above. A key difference, however, is that many fault compartmentalization studies use fault rock property data that was collected under inappropriate laboratory conditions. For example, many studies use fault rock permeability data collected at ambient confining pressures using brine compositions that are not compatible with the formation despite a wealth of evidence to suggest that the permeability of tight rocks is very sensitive to the stress conditions (e.g. Thomas and Ward, 1972) and the brine chemistry (e.g. Lever and Dawe, 1987). The current study differs in that fault rock permeability measurements were made at high stresses using formation compatible brines. The new fault rock permeability data has then been incorporated into the dynamic reservoir simulation model to improve production forecasts.

Reservoir

The main reservoir is in Late Jurassic sandstones of the Heather Formation. The reservoir is comprised of turbiditic sandstones, deposited syntectonically, during the main rifting event in the Late Jurassic. The reservoir is currently located at a depth between 2400m – 2800m, with the temperature at reservoir level being slightly above 90^{o} C. Glacial melting during Pleistocene times resulted in an uplift of approximately 300m. The reservoir thickness varies between 10m and 130m (mean 60m). The N/G of the reservoir section varies between 55% and 73%. The reservoir permeabilities range from 0.1 – 5 Darcy and porosities vary between 10% and 30%. The reservoir experienced the precipitation of early K-feldspar overgrowths and kaolin during shallow burial. Mechanical compaction was the main process for reducing porosity and permeability during intermediate burial. The sandstones experienced small amounts of quartz precipitation and grain contact quartz dissolution during deep burial.

Structural setting

The field is compartmentalized by numerous seismic scale, mainly NW-SE and NE-SW striking, normal faults (Fig. 1a). East-West striking faults are present, but to a minor amount. The maximum fault throw observed is around 60m with a mean around the seismic resolution of 25m. The main reservoir is self-juxtaposed throughout the field (Fig. 1b), implying that the properties of the fault rocks need to be considered to predict the impact of faults on fluid flow during production. It is important to note that no evidence of a static fault seal over geological time exists within the main part of the field. The wells drilled in the main part of the field, e.g. well A, B, D, have pressures on a common gradient, which is consistent with communication through the hydrocarbon phase. However, this cannot be taken as evidence that the faults will not impact flow on a production time-scale. The hydrocarbon water contact has been drilled in well B, whereas the wells A and D have an oil- and gas-down-to.

Deposition of the reservoir happened syntectonically and the turbidites were deposited in half grabens (Figs 2, 3). Faulting started in the Late Triassic and continued throughout the Early and Middle Jurassic, with the main rifting in the Late Jurassic. In general, the tectonic activity ceased in the Latest Jurassic, but some faults are active in the Early Cretaceous (Fig. 2). Structural restoration indicates that the faulting that affected the reservoir occurred at relatively shallow depths (<1000m).

The main fault network only represents faults that could be mapped over a larger distance and continuously on seismic sections. It shall be pointed out that the seismic quality, even after reprocessing is only fair to poor in the field area, which adds uncertainties to the fault interpretation. The intensity of seismic scale faulting differs around the four wells (well A = 4faults/km^2, well B = 2 faults/km^2, well C = 4 faults/km^2, well D = 1 fault/km^2). Seismic attribute analysis (ant-tracking, Fig. 4) in combination with core and borehole image analysis data (Fig. 5a) suggest a denser fault network (well A = 2 faults/km^2, well B = 10 faults/km^2), which is not represented by a visible offset of horizons at the current seismic resolution. Well A drilled right through one of the faults identified on seismic attribute analysis (Fig. 4). Plotting fault zones identified from borehole image analysis on seismic sections at the well location indicates that many small scale faults are only subtle or not at all visible on the seismic (Fig. 5b). Similar features as in well A are also observed in well B. Very few small-scale faults are recorded in borehole image logs and cores in the southern well C and D at the reservoir level, although those are also located very close to seismic scale faults. No reliable results from the attribute analysis could be obtained due to the poorer quality of the seismic around the two wells.

Fault rock property analysis

Fault rock samples

The complete reservoir section has been cored in the wells A and B and the samples analysed in this study were taken entirely from these two cores. Two fault zones with unknown offsets are visible in well A (Fig. 6, see also Fig. 5a). It seems appropriate to expect similar fault styles observed in the fault rock samples also at a larger scale in the reservoir-scale faults. Figure 7a shows multiple faults on a small scale, which reflects the observations made on the seismic and borehole images. The fault propagates upwards, nucleating at the lower left and fault splays are developed in the more shale-rich section (between 37m and 33cm). The fault continues with a clearly visible offset of a distinctive shale band (29cm). A small clay smear is developed, resulting from the smearing of the fine clay-rich laminations within the sand-rich interval. In the clean sandstones above and below the clay-rich band, the clay content of the fault rock seems to be significantly lower. This is likely to represent the fault rock properties expected in the self-juxtaposed cleaner sandstones section for the reservoir scale faults. A small half-graben is present towards the top of Figure 7a, which is infilled with coarser material. The cored faults in more shale-rich layers often show partial clay smear, or at least a clay-rich fault rock (Fig. 7b, c). It is, however, apparent from the sampled faults that clay smears are often discontinuous. It is occasionally observed that the fault dip flattens in the more shale-rich lithologies at the seismic scale (Fig. 3). The same phenomena, caused by geomechanical heterogeneities, is also observed at a small scale in the cored faults, where the dip of the fault surface becomes less steep in the more clay-rich layers (Fig. 8a). Deformation bands are commonly observed features and the fact that no grain fracturing has occurred during faulting indicates that they were formed during shallow burial (Fig. 8b, c).

A bias exists for the fault rock samples. In the more heterogeneous section the sample integrity has been an issue, so only faults in the more homogenous, sandier section could be sampled. This implies that faults in impure sandstones and in clay-rich layers are under-represented.

Analytical procedures

Extensive laboratory work was undertaken on selected fault rock samples from two wells (A & B) including CT-scanning, SEM-analysis, absolute permeability analysis, and quantitative XRD (QXRD). The individual techniques are described in more detail below.

Sample preparation

Typically, 10 to 20 cm sections of core containing the faults were carefully wrapped and sent to the laboratory for analysis. On arrival, the samples were photographed and CT scans were taken using a Picker PQ 2000 medical-style scanner to identify the orientation of faults present and whether or not there were obvious signs of damage generated during coring or following coring. The CT scans allowed us to identify the optimal orientations to take samples for further analysis. A range of subsamples were required for microstructural and petrophysical property analysis of the fault rock present and its associated undeformed sandstone including:-

- Core plugs of the host and fault rock; the latter were orientated perpendicular to the fault so that fluid was forced to flow across the fault during analysis. It is generally preferred to take 25.4 or 38.1 mm core plugs but the core was too thin so 16 and 20 mm core plugs were taken and these were analysed in purpose built core holders.
- Cubes of fault rock and host sandstone, around 1 to 1.5 cm^3, were cut for permeability analysis. The sample containing the fault rock were cut and set in dental putty in an orientation that meant that fluid had to flow through the fault rock during permeability analysis. The use of dental putty means that it is not possible to apply high confining pressures to these samples during permeability analysis.

- Around 1.5 x 1.5 x 0.5 cm samples containing fault rock and the associated host sandstone were cut for microstructural analysis.
- A 1cm^3 sample representative of the host sandstone was then taken for QXRD analysis. This analysis was not performed on the fault rocks as they were too narrow to be sampled. The fault throws are very low so it was assumed that the mineralogy of the fault is the same as the host sandstone, which is consistent with microstructural observations.

All samples were cleaned in a Soxhlet extractor using a 50:50 mixture methanol-toluene/dichloromethane and then dried in a humidity controlled oven at 60^{o}C.

SEM analysis

The blocks for microstructural analysis were impregnated with a low viscosity resin, ground flat with progressively finer grades of diamond culminating in a polish using 1 μm diamond paste. The samples were then coated with a 10 nm thick layer of carbon before being analysed using a FEI Quanta 650 FEGESEM environmental SEM with Oxford Instruments INCA 350 EDX system/80mm X-Max SDD detector, EBSD and KE Centaurus EBSD system. The mineralogy and diagenetic history of the samples was determined as well as the fault rock microstructure and timing of faulting relative to the diagenetic history. BSEM images were stored as 8 bit TIFF files so that they could be incorporated into an image analysis package and their mineralogy quantified.

Permeability analysis

Permeability measurements were made using two methods. One set of measurements were made at ambient stress using distilled water as the permeant so the results could be compared to those from previous studies of the permeability of fault rocks (e.g. Fisher & Knipe, 1998; 2001). In these cases, the cleaned cubes were set in dental putty so that they could be confined at 70 psi confining pressure in a steady-state water permeameter. The samples were saturated with distilled water, placed in the permeameter before using syringe pumps to establish steady-state flow. The permeability was calculated using Darcy's law based on the flow rate, sample length and area, the upstream and downstream pressure differential and the viscosity of the water. The samples containing fault rock also contained undeformed sandstone so the fault permeability was deconvolved from the measurements assuming that the permeability measured was the thickness weighted harmonic average of the fault rock and the host sediment.

The second set of measurements were made on core plugs at higher stresses using formation compatible brine. Coreholders were specially constructed for the sample analysis as we could only obtain 16 and 20 mm diameter core plugs, which are far narrower than the 25.4 and 38.1 diameter cores normally analysed. The core plugs were trimmed so that the ends were flat and orientated perfectly perpendicular to the axis of the core plug. Formation compatible brine permeabilities were measured under stresses of 500psi, 1500 psi, 2000psi, 2500psi, 3000psi, 4000psi, 5000psi. These high stresses close microfractures created as core samples are brought to the surface following coring. Samples with permeabilities of >0.1 mD were measured using the steady-state technique whereas samples with lower permeabilities were measured using the pulse-decay method. As with ambient stress measurements, core plugs containing fault rock also contained undeformed sandstone so the fault permeability was deconvolved from the measurements assuming that the permeability measured was the thickness weighted harmonic average of the fault rock and the host sediment.

QXRD analysis

The intensity of a X-ray diffraction pattern of a mineral is proportional to the amount present within a mixture (e.g. Hardy & Tucker, 1988). On this basis, XRD has frequently been used to quantify the proportions of minerals present within rocks. One method to make such analyses is to construct calibration curves based on the XRD analysis of mixtures containing different proportions of an internal standard such as corundum. The technique requires preparation of samples with complete random orientation (Brindley, 1984). Sample preparation has, however, proved such a difficult task that the technique has been widely regarded as semi-quantitative at best (Hillier, 1999). Recently, a spray dry technique has been developed that appears to produce samples for XRD analysis without significant preferred orientation - even when they contain significant proportions of clays (Hillier, 1999; 2000). The technique involves grinding the sample with a standard (20 wt. % corundum) and then spraying a slurry of the mixture through an air brush into a tube furnace to form ~30 µm wide spherical aggregates with random mineral orientation. The spheres are then top loaded into a specimen holder and then analysed using XRD. The diffraction results obtained are analysed by either reference intensity ratio (RIP) or a Rietvold method to produce mineralogical analyses that are accurate at the 95% confidence level to $\pm X^{0.35}$, where X is the concentration in wt. %. QXRD data is presented as a percentage of the rock volume (including porosity) so is consistent with previous studies (e.g. Fisher and Knipe, 1998, 2001).

Microstructure, mineralogy and petrophysical property results

QXRD analysis indicates that the host sediments contain 54 to 73.4% quartz, 3 to 7.2% albite, 11.4 to 18.7% microcline, 1.4 to 4.4% mica, 1.4 to 17% kaolin and small amounts (<1%) of pyrite. The undeformed sandstones have a diagenetic history that is typical of Jurassic sandstones in the North Sea that have been buried to 2800 m. In particular, they have experienced the precipitation of early K-feldspar overgrowths and kaolin during shallow burial. Mechanical compaction was the main process for reducing porosity and permeability during intermediate burial. The sandstones then experienced small amounts of quartz precipitation and grain contact quartz dissolution.

Examination of the structure of the samples in core suggested that most of fault rock samples are phyllosilicate-framework fault rocks (PFFR, Fisher & Knipe, 2001). Microstructural analysis confirms that PFFR are common (Fig. 9) but also indicates that protocataclasites, occasionally with a PFFR border (Fig. 10) and to a minor extent cataclasites were also present. In general, many of the samples had 12 to 18% clay, which places them on the border between clean (<15% clay) and impure (>15% clay) sandstones. So the fault rocks that they contained tend to have characteristics of those expected generally formed from clean sandstones (i.e. domains with pore space that is free from clay) whilst other characteristics are typical of faults formed from impure sandstones (e.g. domains with macroporosity being filled by clay as well as having experienced enhanced grain-contact quartz dissolution); this makes a clear classification of the fault rocks difficult. It should be noted that PFFR's were originally defined as having flow properties that were controlled by presence of a continuous phyllosilicate-rich matrix between the framework grains (Knipe et al., 1997). Later a generalization was made that such fault rocks tend to occur in sandstones containing 15-40% clay (Fisher and Knipe, 1998, 2001). However, the clay content of 15-40% should not be viewed as fixed values. Indeed, the discussion on clay mixing models presented below highlights how the sorting of the sand grains, which make up the framework of fault rocks, has a major impact on their petrophysical properties.

The ratio of the host rock and the fault rock absolute permeabilities is an important parameter that describes the retardation of fluid flow by faults (Yaxley, 1987). Figure 11 shows the data measured from the field and a range of data points from an in-house database from the same area that have the same stratigraphic range and burial depth. Both datasets were measured under ambient stress using distilled water as the permeant. The results demonstrate a permeability reduction of up to three orders of magnitude for the field data. The permeability reductions experienced implies that the fault rocks could have a significant impact on the single-phase flow especially when situated near to a production or injection well. The acquired data from the field fit well into global range, although the permeability reduction seems to be slightly less than in the global dataset. The reduction in permeability occurred as a result of a variety of processes including: faulting-induced grain fracturing, faulting-induced mixing of framework grains with phyllosilicate grains and enhanced grain contact quartz dissolution due to the presence of clays at grain contacts. It is apparent that there is no clear relationship between the fault rock type and the permeability reduction. However, the host rock permeabilties in the more impure sandstones are lower than in the clean sandstones, which is in line with previous work. There does not seem to be a correlation between the clay content of the protolith and the permeability reduction (Fig. 11) although dataset from the field itself is rather limited.

The brine permeability of all fault rocks showed a clear stress dependency (Fig. 9 and Fig. 10). In particular, the stress sensitivity of permeability increases as samples become less permeable (Figure 12). Fault rock samples with >0.1 mD permeability at ambient conditions tend experience permeability reductions of a factor of ~2 when confining pressure is increased to in situ conditions. On the other hand, lower permeability fault rocks often experience an order of magnitude reduction in permeability as confining pressure is increased to in situ conditions. The increased stress dependency of permeability with reduced permeability is consistent with permeability measurements made on other low permeability rocks such as tight gas sandstones (Thomas & Ward, 1972; Wei et al., 1986; Kilmer et al., 1987). Extrapolating the power-law relationship between stress and confining pressure to 70psi indicates that previous measurements made at ambient stress conditions are between 2 and 20 times higher (average difference is 5 fold) than those made at high confining pressures. It should be emphasised that much of this stress sensitivity is likely to be caused by presence of grain-scale microfractures that formed during and/or following coring. The permeabilities of fault rock samples are therefore not likely to be as stress sensitive in the subsurface as in the laboratory, because microfractures will not be present in the subsurface and pores with low aspect ratios are not as stress sensitive unless an increase in stress results in brittle failure of the faults.

Fault rock permeabilities not only depend on the stress applied, but also on the fluid composition used during the experiments. The data shown in Figure 13 demonstrate that the permeabilities for a formation compatible brine are around 5 fold higher than for a deionized water, which has been used as the permeant for these type of measurements (Fisher & Knipe, 1998, 2001; Sperrevik et al., 2002).

An important observation made during this work, incorporating a larger fault rock data set from different unpublished sources is that the effects of applying reservoir stress versus ambient stress and using brine versus deionized water cancel each other almost out and almost a 1:1 relationship seem to exist (Fig. 14). This implies that previously published fault rock property data (Fisher & Knipe, 1998, 2001; Sperrevik et al., 2002; Jolley et al., 2007) can be still used with a certain confidence. This will be the subject of a future publication but it is important for the current study as it justifies using the legacy fault rock data along with the new measurement from the field to derive predictive functions for the fault rock permeability versus fault rock clay content for the reservoir scale faults.

It has been pointed out earlier that a sample bias exists, as some faults, particularly the ones with a higher clay content fault rock or with clay smear, could not be sampled, as the samples tend to break apart along the faults. So the sampled fault rocks mainly resemble the low to medium clay content fraction with some that show properties of phyllosilicate-framework fault rocks (Fig. 15). A relationship between the fault rock type and the fault rock permeability exists, despite the fact that differences in permeabilities of up to two orders of magnitude exist for a similar fault rock clay content are measured (Fig. 15). This observation is consistent with earlier published datasets (Fisher & Knipe, 2001; Sperrevik et al., 2002; Jolley et al., 2007).

Reservoir-scale fault property prediction

To calculate the reservoir and small-scale (lineaments from seismic attribute analysis, see Fig. 4) fault properties a structural framework and a static geomodel has been established. The basis for the model is provided by 3D structural interpretation on a PreSDM dataset and a host rock Vclay model based on the Vclay logs from the four exploration wells, applying an appropriate depositional model. The fault rock clay content has been calculated varying the clay content of the host rock model according to the uncertainties from the petrophysical evaluations. Different fault zone clay predictors, such as SGR (Yielding, 2002) and ESGR (Freeman et al., 2010) were assessed. The SGR at any point of the fault is given by a uniform average of the clay contents of the wall rocks that moved past this point (Yielding 2002). In contrast, the ESGR applies an additional weighting function to the averaging, which assumes that clays that are closer to the point of interest contribute more to the fault rocks (Freeman et al., 2010). To link the fault rock permeability to the fault rock Vclay content; SGR/ESGR for reservoir scale faults; different predictive functions were applied. In addition the impact of potential clay smear on the production figures has been evaluated, together with changes in the relationship of fault rock thickness versus fault throw. Variations in fault throw can have a significant effect on the fault rock properties and reservoir/reservoir juxtaposition patterns in the field. Therefore an uncertainty on the throw of 20% has been incorporated.

The majority of the reservoir-scale faults fall into the PFFR domain, followed by clay smears and disaggregation zones/(proto)cataclastic fault rocks (Fig. 17). No significant difference in the distribution is apparent between the fault rock Vclay content when calculated using either SGR (Yielding, 2002) or ESGR (Freeman et al., 2010), with a weighting factor of 1.5, as a fault rock Vclay prediction algorithm. A more detailed analysis of the Vclay distribution on the fault plane reveals that the ESGR algorithm predicts a more discrete distribution of Vclay, compared to the SGR algorithm (Fig. 17). The aim was to verify the influence of the application of the two different algorithms on the final dynamic simulation results.

The fault rock property data acquired during this study are limited in terms of their statistical value as only around 15 samples of small offset faults (<1 cm throw) were analysed and they do not represent the range of reservoir scale fault rocks (see Fig. 16). To have a statistically valid dataset the field data were combined with data from an in-house database, obtained from the same province, same stratigraphic interval and similar burial depth (Fig. 18). The measurements for the additional data were done under 70psi stress and with deionized water as reservoir fluid, which has discussed above are probably fine to use as the use of distilled water appears to compensate for the impact on permeability of making the measurements at low confining pressures. A cross-plot of fault rock permeability vs. clay content for this larger dataset from analogue faults also has a very large amount of scatter as was the case for the measurements made during this study.

Revil & Cathles (1999) demonstrate that the permeability of the sand/clay mixtures, which is essentially what clay gouges represent, is controlled by the proportion of the host-rock sand and host-rock clay present, the porosity and permeability of the sand end-member as well as the permeability of the shale end-member. The porosity of the host-rock sand is controlled by grain sorting. These factors might explain the scatter of the points in the Vclay versus permeability plot (Fig. 18). The objective was to represent the ranges between fault rock Vclay content and fault rock permeability for the reservoir scale faults. A High-, Mid- and Low-fault rock permeability predictive function has been established (Fig. 19a). The functions are based on a model for the permeability of clay-sandstone mixtures (k_m), presented by Revil et al. (2002).

$$k_m = k_{sd}^{1-\frac{V_{cl}}{\emptyset_{sd}}} \times k_{Cfs}^{V_{cl}/\emptyset_{sd}}, 0 \leq V_{cl} \leq \emptyset_{sd}$$

$$k_m = k_{sh} V_{cl}^{3/2}, \emptyset_{sd} \leq V_{cl} \leq 1$$

where, $\emptyset_{sd}$ and k_{sd} are the porosity and permeability of the clay-free sand, k_{sh} is the permeability of the shale end-member and:

$$k_{Cfs} = k_{sh} \emptyset_{sd}^{3/2}$$

V_{cl} is the clay content of the fault rock, e.g. SGR or ESGR for the reservoir scale faults and k_{Cfs} is the permeability of the clay-filled sand at the boundary between the clayey sands and sandy shales (Revil et al., 2002). The three functions were calculated by establishing three sand-clay mixing models, using the parameters in Table 1. A good fit to the data for the three functions becomes apparent (Fig. 19a). The field data, despite there are only few, fall clearly within the Mid- and Low-case scenario from Revil et al. (2002).

Comparing the Revil et al. (2002) High, Mid and Low fault rock permeability functions with algorithms published previously by Sperrevik et al. (2002) and Jolley et al. (2007) for similar conditions (burial depth <3000m) , it becomes apparent that the latter predict a higher permeability of the fault rocks than indicated by the field data (Fig. 19b).

The final input parameter into the reservoir simulator are TMs that are applied to the faces of grid blocks on either side of the fault plane to take into account the impact of faults on fluid flow. The TM calculation, as described by Manzocchi et al. (1999), requires information on the permeability of the undeformed reservoir in each grid block, the fault thickness and the fault permeability. The prediction of the fault rock thickness is one of the most uncertain parameters. There is a significant scatter in the data, but a 1:100 relationship of fault thickness versus throw is commonly used. Freeman et al. (2008) suggest that a 1:66 relationship is more appropriate for seismic-scale faults. Both relationships were incorporated into the calculation of the fault TMs.

An uncertainty also exists in the calculation of the Vclay content for the well logs and hence for the Vclay model as such. A 10% uncertainty has been estimated, based on petrophysical analysis, for the host rock Vclay content and fault rock property cases were calculated accordingly. In addition potential facies variations were taken into consideration in the uncertainty modelling.

Many properties are linked to the fault throw, such as the reservoir juxtaposition pattern, fault rock clay content prediction, the fault rock thickness and ultimately the TM, as the main input into the dynamic simulation. The fault throw is influenced by three main factors, the accuracy of the seismic migration, the quality and resolution of the seismic data and the structural interpretation. In this case, an uncertainty of the throw of 20% has been considered, based on the above mentioned parameters. A variation of the throw in the static geomodel alters the model geometry and sometimes it is difficult to carry this distorted geometry forward in the dynamic simulation. In order to keep the complexity at an acceptable level, it has been decided to calculate only one case for the throw variation, e.g. increase the throw by 20% (throw 120%). An increase in throw is expected to result in a more disconnected reservoir, which would decrease the recoverable volumes and demonstrates a potential “low case” scenario. The effective-cross fault transmissibility (ECFT, Freeman et al., 2010) is used in Figure 20 to illustrate the effects of an increase in throw. The ECFT, which is a normalized cross fault transmissibility, is computed using the harmonic average of the permeabilities of the undeformed foot wall adjacent to the fault, the fault rock and the undeformed hanging wall across the fault. This is done for a specific width of host wall rock on each side of the fault and the fault rock thickness by the local displacement (Freeman et al., 2010). The lower reservoir interval is the one that contributes most to the recoverable volumes. An increase in throw reduces the area where the lower reservoir is self-juxtaposed (Fig. 20a & b). The fact that more zones with elevated ECFT in the area where the lower reservoir in the footwall is juxtaposed against the upper reservoir in the hangingwall occur (compare Fig. 20a and Fig. 20b), does not counterbalance this effect. This becomes evident in the dynamic simulation.

Small scale fault property prediction

In addition to the seismic faults numerous small-scale faults, without a visible offset in seismic exist. These faults can be observed as lineaments on seismic attribute maps (Fig. 4). It has been considered to be important to include these faults into the dynamic simulation model. The faults were mapped as lineaments and vertical fault planes without an offset were constructed in the dynamic model. As no offset is associated with these faults, their TMs cannot be calculated in the same way as for faults with an offset. Therefore a range of single TMs for the entire small scale fault surfaces was calculated, applying a range of fault throw (1m, 5m, 10m, 20m) with the corresponding fault rock thicknesses using a thickness to throw relationship of 1:100. A single average permeability value of 950 mD has been taken for footwall and hangingwall cells, based on a range of core measurements in the reservoir sandstones. A bulk fault zone permeability has been calculated using the harmonic average from the measured fault rock permeabilities from the cores, using a 30% salinity brine and applying a stress of 4000psi. The harmonic average was used as the permeability required is that measured perpendicular to the fault. It has been concluded from applying the different scenarios that bulk TMs of 0.001, 0.01 and 0.1 represent a realistic range for the small scale faults.

At this stage of the analysis it is important to bear in mind that no history matching data exist in the field, which would allow a calibration of the results. It is important at this point in time to figure out which parameters have the most significant impact on the resulting recoverable volumes. Once history matching data are available this provides a good basis for a more focused analysis of the key influencing parameters.

A summary of the cases that were incorporated into the dynamic simulation is given in Figure 21.

Simulation modelling results

The scenarios discussed above were, together with other geological variables, incorporated into a fully integrated, automated workflow for dynamic reservoir simulation and uncertainty modelling (200 iterations). The main goal was to identify which one of the many parameters, apart from the fault properties, in the uncertainty model have the most impact on the recoverable volumes and the recovery efficiency. An additional objective was to verify the impact of the different fault property cases on the recoverable volume range. In order to ensure that the results are comparable, the producer/injector well pattern has not been changed during the uncertainty simulation.

In Figure 22 the impact of the several calculated scenarios on the recoverable volumes is highlighted. In case a TM = 1 is applied, the recoverable volumes are as if there were no faults present, e.g. normalized to

100%. If the minimum case of recoverable volumes is valid, e.g. if low permeable seismic scale faults combined with low permeable small scale faults are present, the recovery would be only 70% compared to a model without faults. The dynamic simulation reveals that the clay content versus permeability relationship, together with variations in fault throw, have the most significant impact on the recoverable volumes (Fig. 22). Slightly tighter faults are predicted when the ESGR is used as a mixing algorithm. The impact of a thickness to throw ratio of 1:66 instead of 1:100 leads to a decrease in fault transmissibility, but not to a significant amount. The presence of clay smear does not lead to significantly tighter faults and hence causes only a minimal reduction in recoverable volumes because continuous clay layers are not predicted in the host rock model. The functions suggested by Sperrevik et al. (2002) and Jolley et al. (2007) seem to predict less influence of the faults on the subsurface fluid flow for this particular case. The incorporation of small-scale faults whose throw cannot be mapped can decrease the recoverable volumes again by up to 10%, compared to the cases where only the larger scale faults are taken into consideration. Combining the observations made on core-scale, with seismic attribute analysis strongly suggests the need to incorporate the small-scale faults into the model. The dynamic simulation with several fault property scenarios shows that a reduction between 10% and 30% of the recoverable volumes, compared to a model without or completely open faults, is likely.

The impact of the faults on the recovery efficiency and cumulative production were assessed in the uncertainty modelling. Apart from the fault properties, other parameters such as the variation on top and base reservoir grids, residual oil and water saturation and reservoir porosity and permeability were incorporated into the analysis. The properties of the faults are among the most influential parameters for the oil recovery efficiency. Using fault specific TMs, generated applying the above discussed workflow, versus a distribution of single TM values reduces the uncertainty by around 40% for the recovery efficiency. This is a very important result as it clearly demonstrates the value of a detailed fault analysis compared to just using single global values.

For the cumulative production the fault properties are an important, but not the most influential parameter. Again, using a fault specific TM grid, based on the above described fault analysis workflow, compared to applying a range of single TM reduces the uncertainty by 50%.

Discussion

The seismic interpretation, which is a key element that provides the basis for a quality fault analysis and the translation of the interpretation into the static geomodel, has not been discussed in detail in this paper. The seismic data quality across the field is only fair, which implies that that the fault and horizon picking is associated with uncertainties; the same is also true for the velocity model. The possibility to run fully integrated uncertainty models really helped to incorporate these different parameters and assess their impact. However, a verification of effects from different interpretation concepts is not possible within this workflow, but would be a subject for further analysis, once the field is in development and history matching data exist, which allow a better calibration of the outcomes.

Similar fault styles are observed on core and seismic scale (compare Figure 2 with Figure 8). The availability of numerous fault rock samples from core, together with high quality borehole images was a real benefit for the work. In the first instance, these data highlight the complexity of the faulting, also below seismic resolution. Secondly, the fault rock data provide the basis for the calibration of the reservoir-scale fault rock permeability prediction. As demonstrated, the results from the absolute permeability measurements on these samples under reservoir stress conditions, using a reservoir compatible fluid are very similar to absolute permeability measurements under ambient stresses but using deionized water as a permeant (Fig. 14). It shall be pointed out, that this observation does not imply that the efforts for conducting measurements under realistic subsurface conditions are not necessary in the future, but highlights the possibility to use previously acquired datasets with a certain confidence.

We find that the functions developed by Revil et al. (2002) provide an appropriate description for sand-clay mixtures (fault rocks) and their related absolute permeabilities. Revil & Cathles (1999) demonstrate that the permeabilities of these mixtures are not only a function of the clay content, as suggested by previous authors (Fisher& Knipe 1998; Fisher & Knipe 2001). Functions that correlate the fault rock clay content to the fault rock permeability suggested by Sperrevik et al. (2002) and Jolley et al. (2007) seem to predict a lower impact of the faults on the subsurface fluid flow in this specific case. This can be due to various factors including:

i. The functions suggested by Jolley et al., (2007) and Sperrevik et al., (2002), which were used in this paper for comparison, are derived from regression lines through a cloud of data with a significant scatter for a given depth of burial. This implies that the high- and low-side will not be fully represented.

ii. **The** measurement setup, e.g. permeability measurements with deionized water at ambient stress does not represent real subsurface conditions, e.g. reservoir compatible brine at subsurface stress.

iii. The data used by Jolley et al. (2007) and Sperrevik et al. (2002) are not from the field, so the use of specific field data should provide more accurate ranges.

iv. The sand-clay mixing model proposed by Revil & Cathles (1999) appears to be a proper representation of the parameters that lead to the development of fault rocks and their properties..

It has been pointed out already that the work described in this paper lacks the calibration of the fault analysis results by history matching data or even long term well tests. Once the field is under development and production data exist, the exercise will have to be repeated and it is expected that the uncertainties can be significantly reduced. In any case, the current study provides a good basis for future work.

Conclusions

A better understanding of the fault properties by incorporating geologically sensible parameters played an important role in the uncertainty assessment for the field development planning. In this context the incorporation of fault rock measurements from field data, together with application of the algorithms from Revil et al. (2002) for the fault rock clay content prediction increased significantly the credibility of the analysis results. The fault properties are among the most critical and influential parameters especially for the recovery efficiency, but also for the cumulative production. It can be demonstrated that using a fault specific transmissibility multiplier grid versus a distribution of single, global transmissibility multiplier values significantly reduces the uncertainties for the recovery efficiency and cumulative recovery.

Acknowledgements

The authors thank Wintershall Norge AS, Capricorn Norge AS, Bayerngas Norge AS, DEA Norge AS, Repsol Norge As, Edison Norge AS and Explora Petroleum AS, for the permission to publish this paper. We also thank Eriksfiord and the CiPEG Leeds for the permission to present data generated by them for this study.

References

Brindley, G.W. (1984) Quantitative X-ray analysis of clays. Pp. 411-438 in: Crystal Structures of Clay Minerals and their X-ray Identification (G.W. Brindley & G. Brown, editors). Mineralogical Society, London.

Fisher, Q. J. & Knipe, R. J. 1998. Fault sealing processes in siliciclastic sediments. In: G. Jones, Q. Fisher and R. J. Knipe (eds) Faulting and Fault Sealing in Hydrocarbon Reservoirs. Geological Society, London, Special Publication, **14**, 117-134.

Fisher, Q. J. & Knipe, R. J. 2001. The permeability of faults within siliciclastic petroleum reservoirs of the North Sea and Norwegian Continental Shelf. Marine and Petroleum Geology, **18**, 1063-1081.

Fisher, Q.J. & Jolley, S.J. 2007. Treatment of faults in production simulation models. In: Jolley, S. J., Barr, D., Walsh, J. J. & Knipe, R. J. (eds) Structurally Complex Reservoirs. Geological Society, London, Special Publications, **292**, 219-233.

Freeman, S.R., Harris, S.D. & Knipe, R.J. 2008. Fault seal mapping – incorporating geometric and property uncertainty. In: Robinson, A., Griffiths, P., Price, S., Hegre, J. & Muggeridge, A. (eds) The Future of Geological Modelling in Hydrocarbon Development. The Geological Society, London, Special Publications, **309**, 5-38.

Freeman, S.R., Harris, S.D. & Knipe R.J. 2010. Cross-fault sealing, baffling and fluid flow in 3D geological models: tools for analysis, visualization and interpretation. Geological Society, London, Special Publications, **347**, 257-282.

Hardy, R. & Tucker, M.E. 1988. X-ray diffraction. In: Tucker, M. E. (eds) Techniques in Sedimentology. Blackwell, Oxford, 191-228.

Hillier, S. 1999. Use of an Air Brush to Spray Dry Samples for X-Ray Powder Diffraction. Clay Minerals, **34**, 127-135.

Hillier, S. 2000. Accurate quantitative analysis of clay and other minerals in sandstones by XRD: comparison of a Rietveld and a reference intensity ratio (RIR) method and the importance of sample preparation. Clay Minerals, **35**, 291-302.

Jolley, S.J., Dijk, H., Lamens, J.H., Fisher, Q.J., Manzocchi, T., Eikmans, H. & Huang, Y. 2007. Faulting and fault sealing in production simulation models: Brent Province, northern North Sea. Petroleum Geoscience, **13**, 321-340.

Kilmer, N.H., Morrow, N.R., and Pitman, J.K. 1987. Pressure sensitivity of low permeability sandstones. Journal of Petroleum Science and Engineering, **1**, 65-81.

Knipe, R. J., Fisher, Q. J., Jones, G. , Clennell, M. R., Farmer, A. B., Kidd, B., McAllister, E., Porter, J. R. & White, E. A. 1997. Fault seal analysis, successful methodologies, application and future directions. In: Møller-Pederson, P. & Koestler, A. G. (eds) Hydrocarbon Seals - Importance for Exploration and Production. Norwegian Petroleum Society (NPF), Special Publication, **7**, 15-37.

Lever A., and Dawe, R.A. 1987. Clay migration and entrapment in synthetic porous media. Marine and Petroleum Geology, **4**, 112-118.

Manzocchi, T., Walsh, J.J., Nell, P. & Yielding, G. 1999. Fault Transmissibility Multipliers for flow simulation models. Petroleum Geoscience, **5,** 53–63.

Revil, A. & Cathles L.M. 1999. Permeability of shaly sands. Water Resources Research, **35**, 651-662.

Revil, A.C., Grauls, D. & Brevart, O. 2002. Mechanical compaction of sand/clay mixtures, Journal of Geophysical Research, **107**, (B11), 2293.

Sperrevik, S., Gillespie, P.A., Fisher, Q.J., Halvorsen, T. & Knipe, R.J. 2002. Emperical Estimation of Fault Rock Properties. In : Koestler, A. G. & Hunsdale, R. (eds) Hydrocarbon Seals Quantification. Norwegian Petroleum Society (NPF), Special Publication, **11**, 109-125.

Thomas, R.W. & Ward, D.C. 1972. Effect of Overburden Pressure and Water Saturation on Gas Permeability of Tight Sandstone Cores, JPT, 120.

Wei, K.K., Morrow, N.R. & Brower, K.R. 1986. Effect of Fluid, Confining Pressure, and Temperature on Absolute Permeabilities of Low-Permeability Sandstones, Society of Petroleum Engineers, Formation Evaluation, 413.

Yaxley, L.M., 1987. Effect of a partially communicating fault on transient pressure behaviour. Society of Petroleum Engineers, Formation Evaluation, 590–598.

Yielding, G. 2002. Shale gouge ratio – calibration by geohistory. In : Koestler, A. G. & Hunsdale, R. (eds) Hydrocarbon Seals Quantification. Norwegian Petroleum Society (NPF), Special Publication, **11**, 1-15.

Figure captions

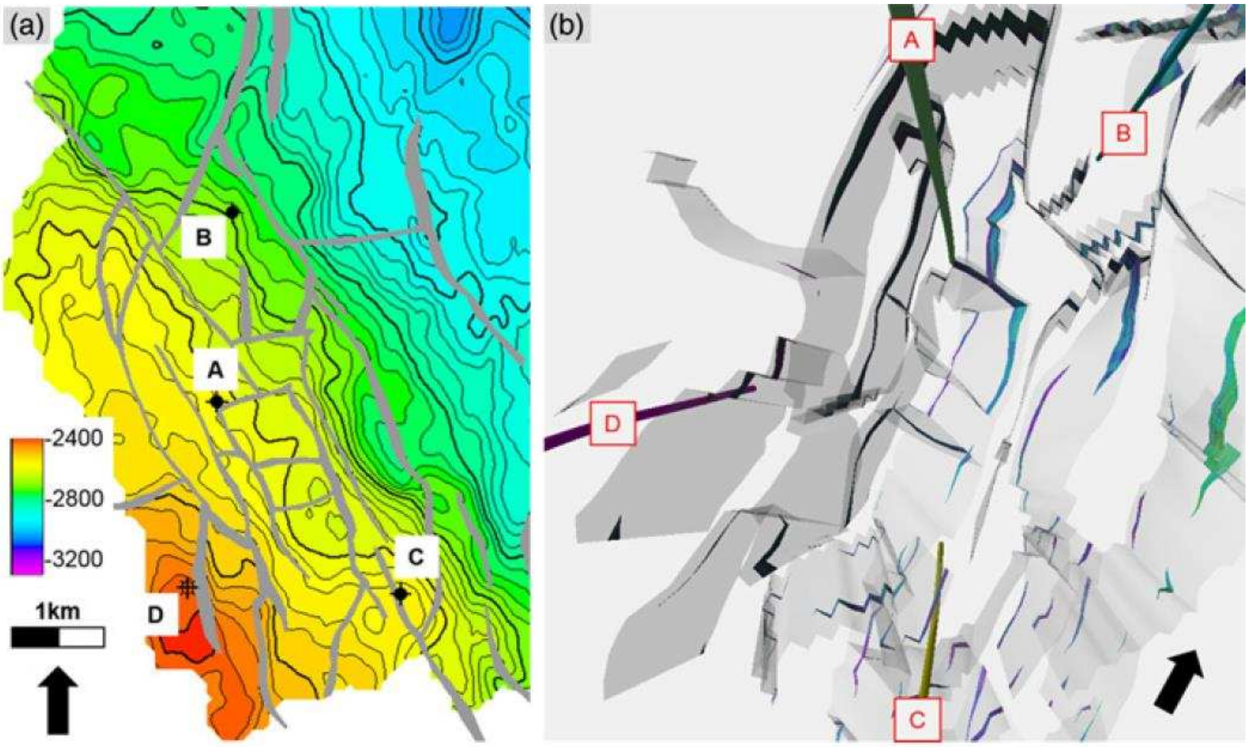

Fig. 1 (**a**) Top reservoir depth map with the four exploration/appraisal wells (A-D) and the fault polygons (**b**) 3D fault model from the static geological model (view from above), colored areas (SGR) highlight reservoir/reservoir juxtaposition.

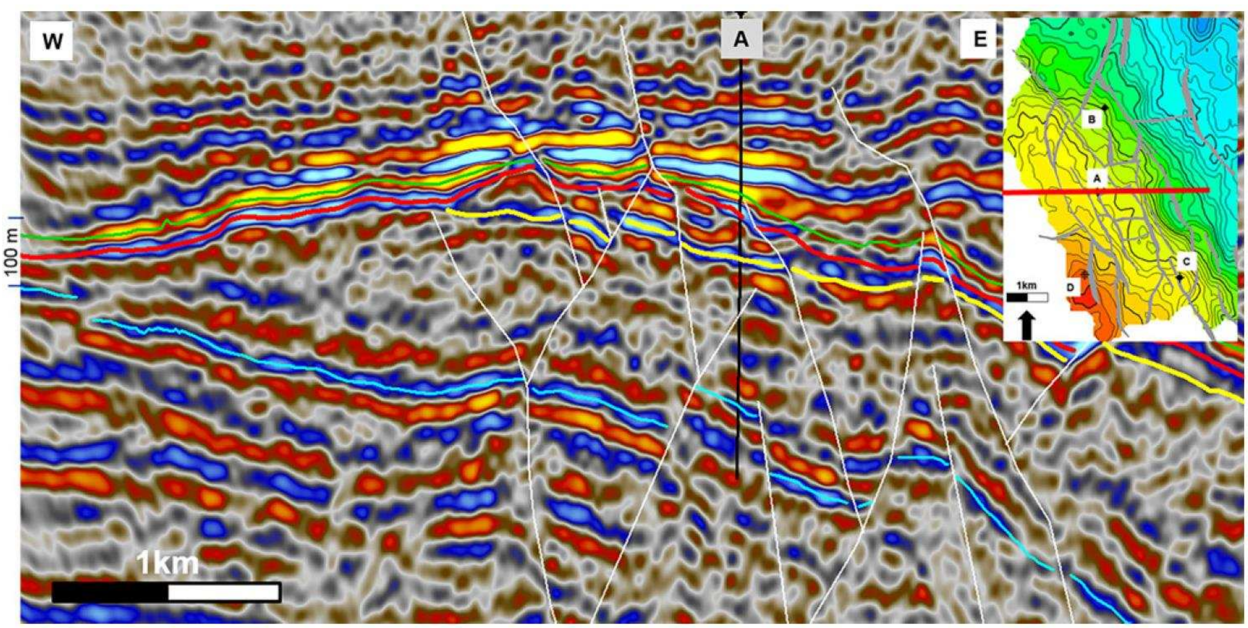

Fig. 2. Depth seismic section across the field, highlighting the structural complexity at reservoir level. Note that most faults predate the unconformity (red horizon), but some also seem to have

younger movements. Green horizon = Base Crecateous Unconformity, red horizon = near top reservoir and unconformity, yellow horizon = base reservoir, blue horizon = Top Brent Gp.

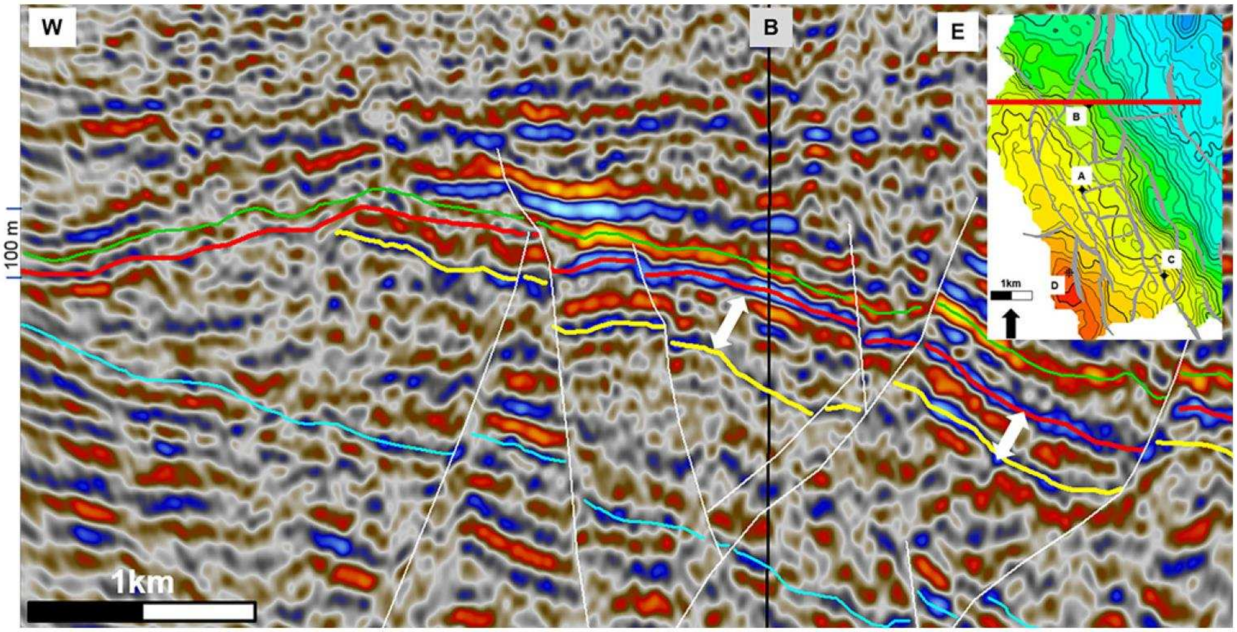

Fig. 3. Depth seismic section across the field, highlighting the structural complexity at reservoir level. Note that most faults predate the unconformity (red horizon), but some also seem to have younger movements. Note the thickening across the faults (white arrows), indicating syntectonic deposition. Occasionally a dip refraction of the faults in the more shale rich lithologies between the base reservoir and top Brent Gp is visible. Green horizon = Base Cretaceous Unconformity, red horizon = near top reservoir and unconformity, yellow horizon = base reservoir, blue horizon = Top Brent Gp.

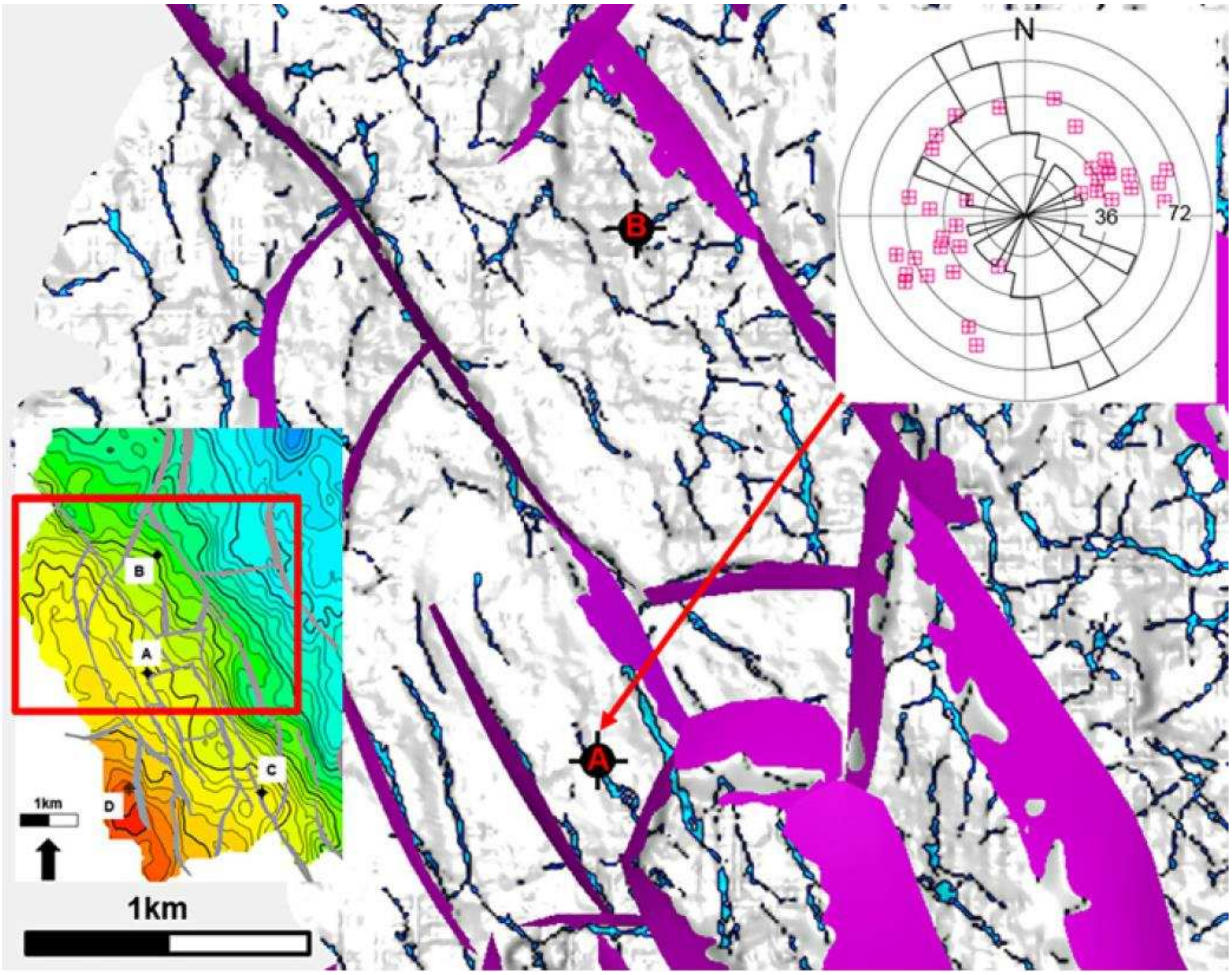

Fig. 4. Seismic attribute (Ant Tracking) map near the base reservoir, showing the main fault planes that were interpreted on the seismic sections (coloured planes) and faults below seismic resolution and without visible offset (blue lineaments). The strike histogram (SCHMIDT, Upper, poles to planes) highlights the orientation of small scale faults identified from borehole image analysis in well A. Note the good correlation with the lineament on the attribute map.

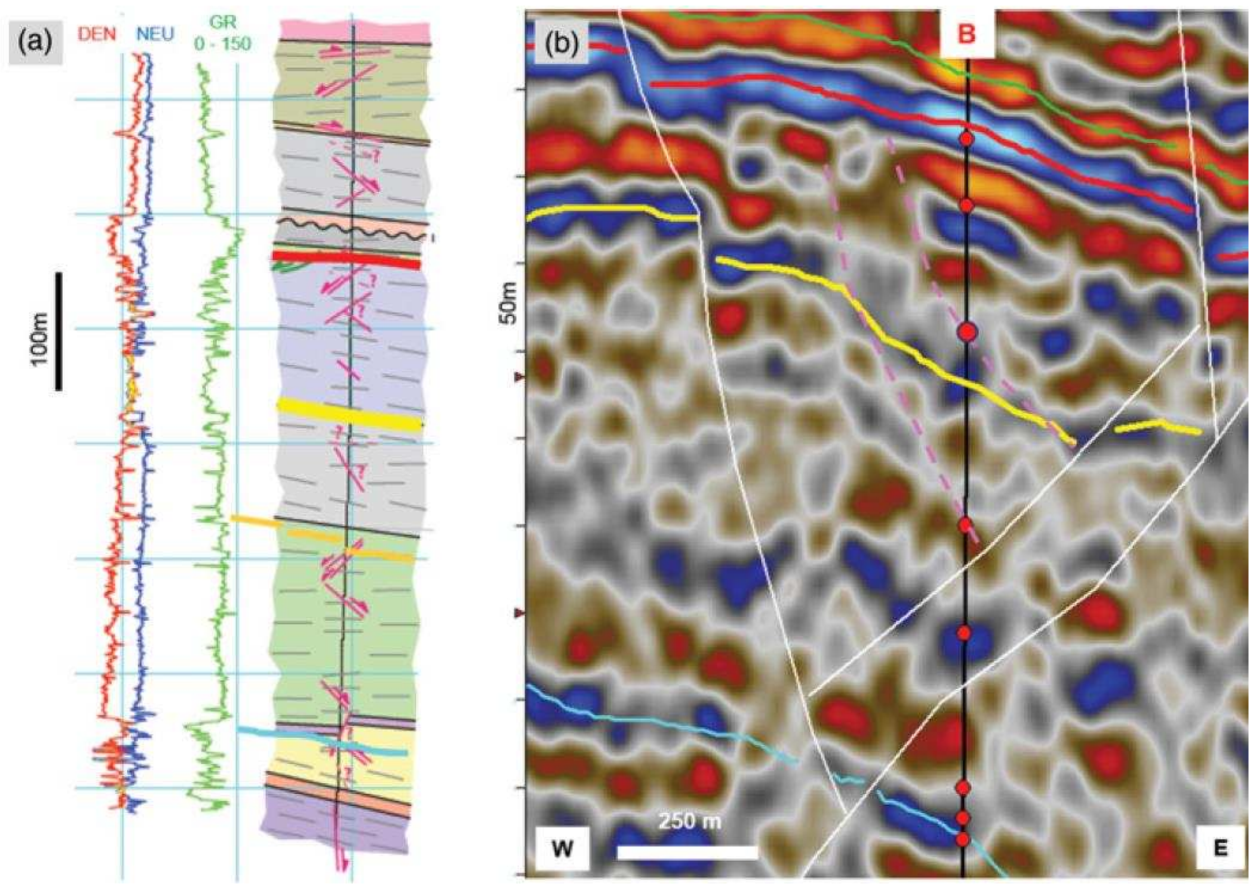

Fig. 5. (**a**) Schematic section through well B highlighting the main lithological units and the faults (magenta) identified on borehole image logs. The colour coding for the horizons is identical to the ones in (b). Near top reservoir = red line, base reservoir = yellow line, blue line = top Brent Gp. (**b**) seismic cross section through well B with the top (red) and base (yellow) of the main reservoir, seismic scale faults (white), sub-seismic scale faults (magenta), red dots highlight faults identified on borehole image logs.

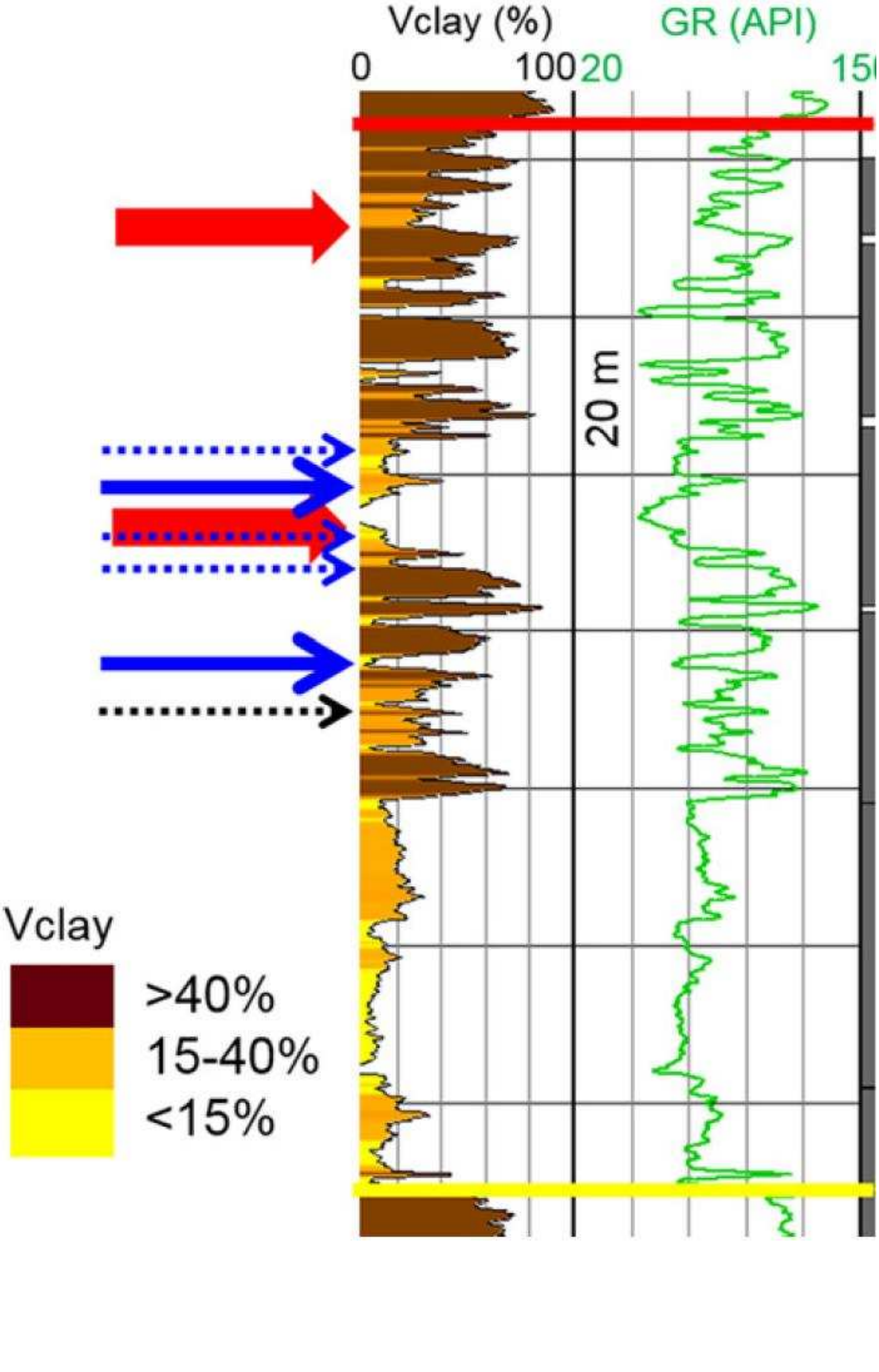

Vclay (%)
GR (API)
0
100
20
150
20 m
Vclay
>40%
15-40%
<15%

Fig. 6. Reservoir section from well B with Vclay and GR log. Bold red arrows = fault zones identified on image log. Solid blue arrows = fault rock samples displayed in Fig. 10 & 11. Stippled blue arrows = additional sampled and analyzed fault rocks. Stippled black arrow = sample in Figure 7c. Red line = top reservoir, yellow line = base reservoir. The grey section on the right side of the log represents the cored intervals.

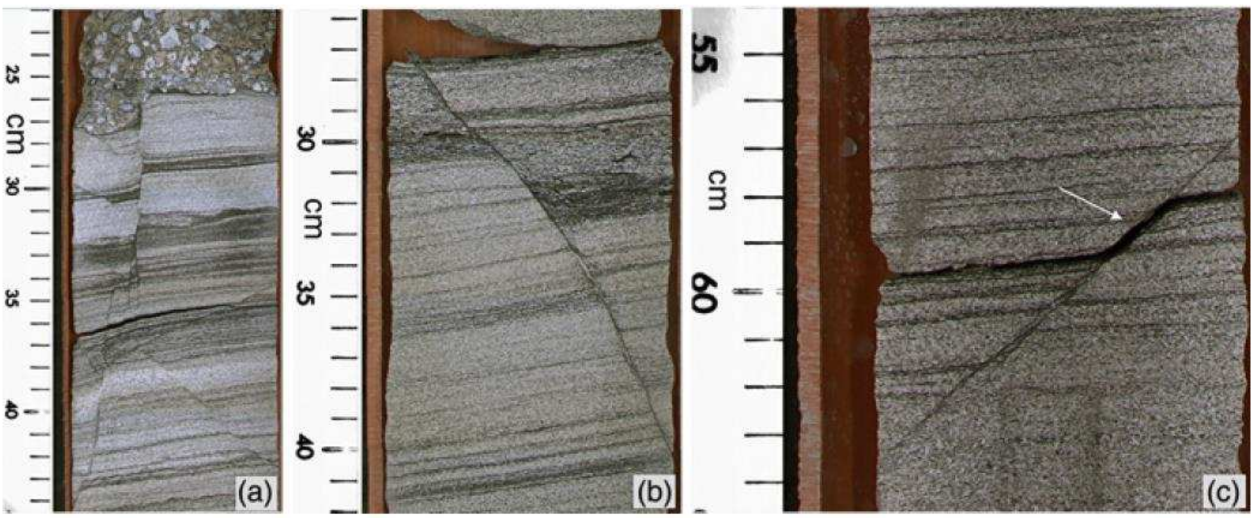

Fig. 7. Cored small scale faults (**a**) Multiple normal faults. (**b**) Single normal fault with cm-offset of a clay-rich layer. The dark colored fault rock is enriched with phyllosilicates. (**c**) Normal fault with a cm-offset of a shale layer, developing a clay smear (white arrow); see also Figure 6 for location.

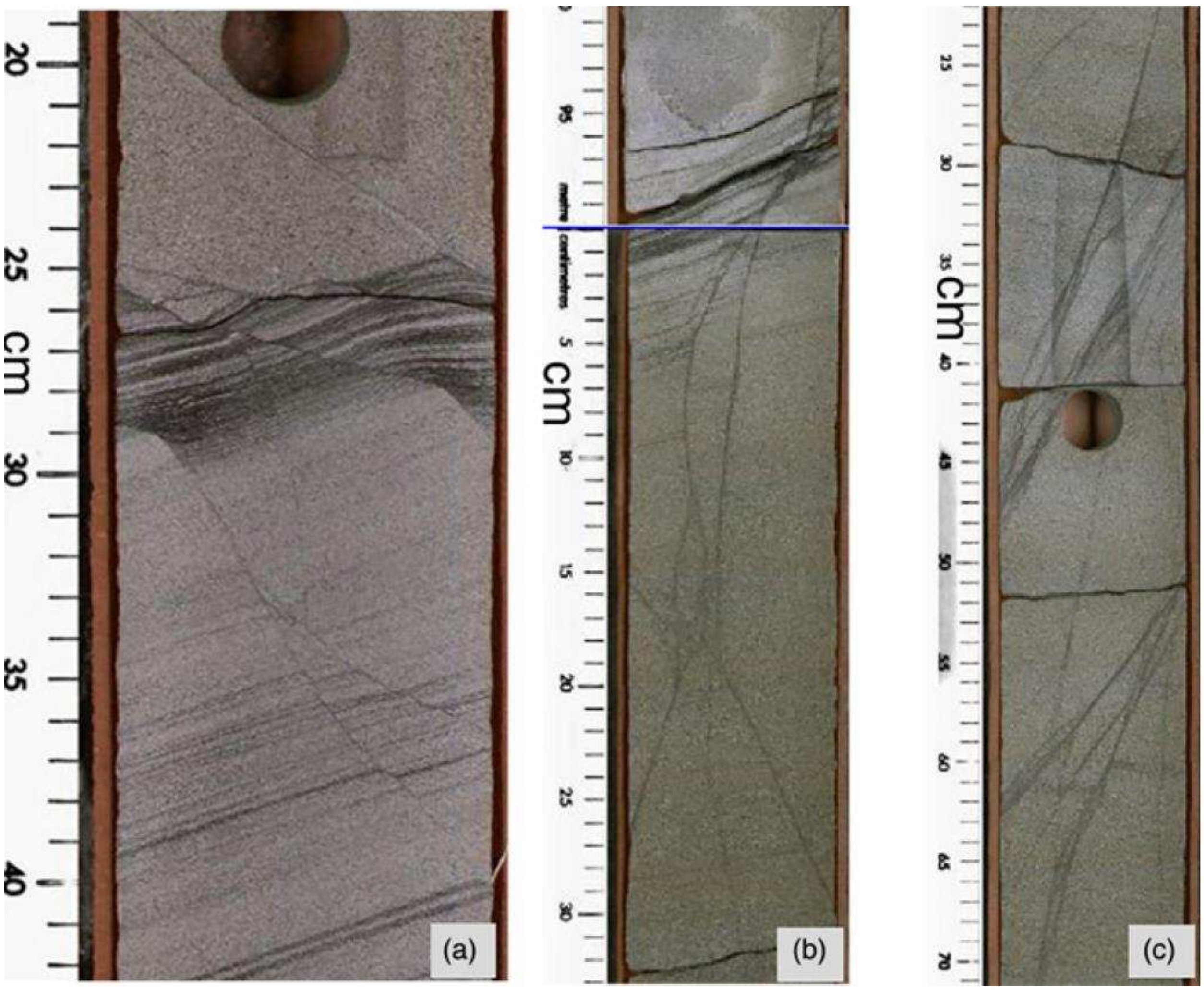

Fig. 8. Cored small scale faults and deformation bands (**a**) Small scale normal faults with cm-offset. Note the influence of the mechanical stratigraphy on the dip-angle of the fault plane. (**b**) Normal faulting in a clay-rich layer and deformation bands without visible offset in a clean sandstone package. (**c**) Deformation bands in a clean sandstone section. The dark color is due to trapped oil, which cannot escape due to the reduced porosity.

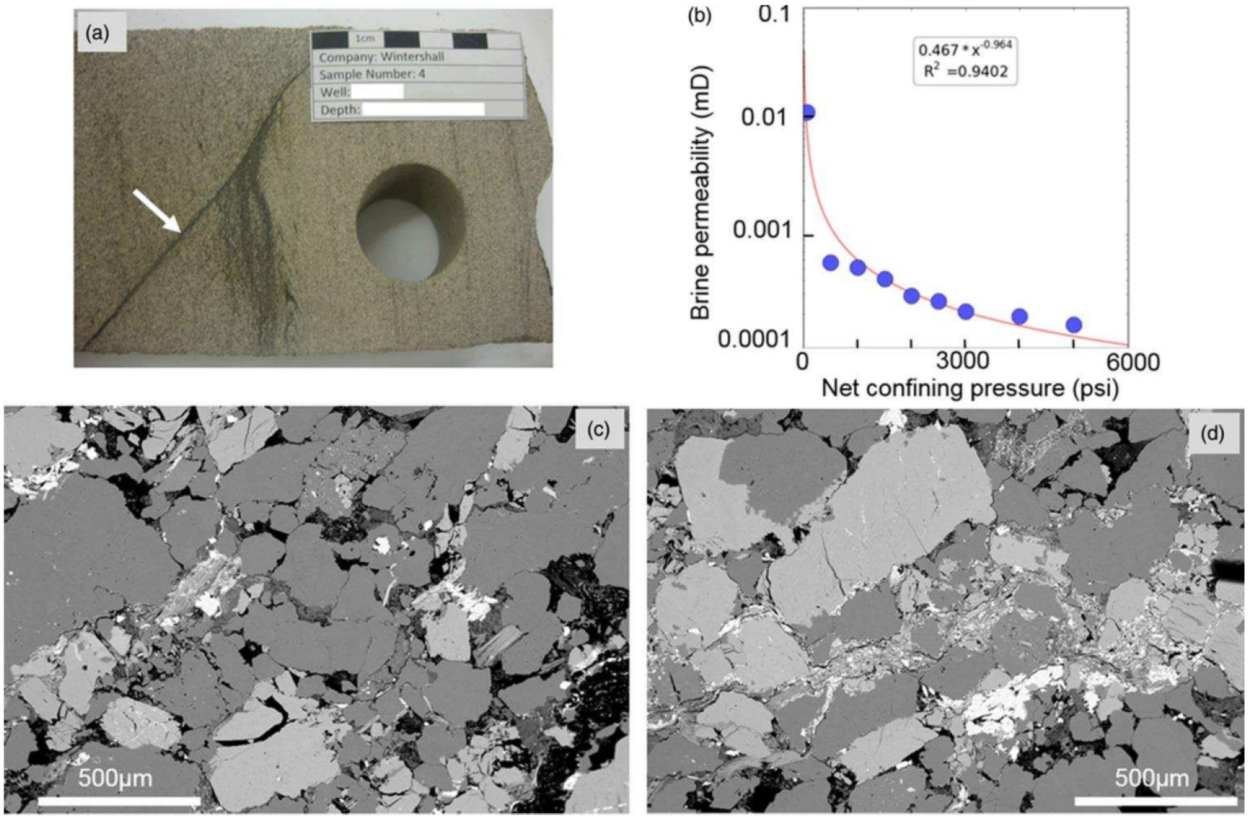

Fig. 9. Phyllosilicate framework fault rock (PFFR) in an impure sandstone. The offset of the fault is not visible. (**a**) core sample with a white arrow showing the position from where the sample for laboratory analysis was taken. (**b**) Results from absolute gas and brine permeability measurements from the host and fault-rock under different stresses. Note the stress-related permeability reduction. (**c**) BSEM image from host rock (**d**) BSEM image from fault rock.

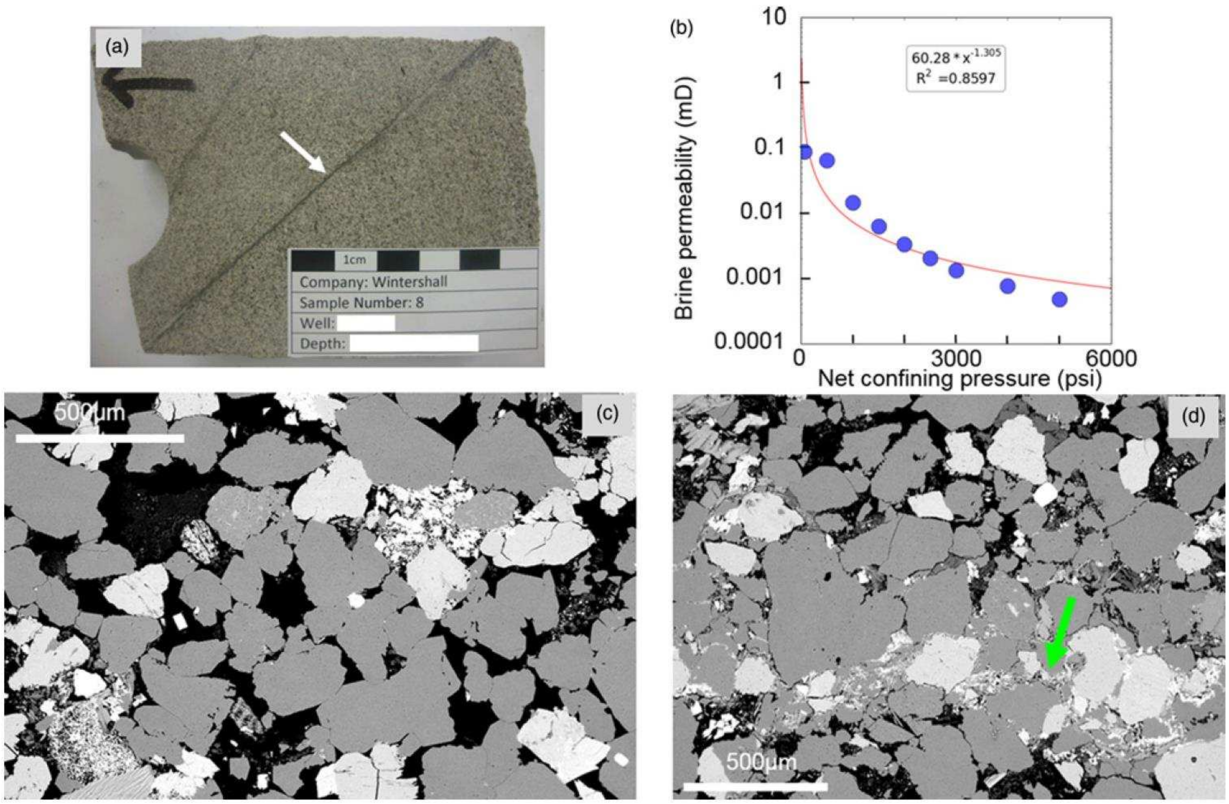

Fig. 10. Protocataclasite with PFFR border in a clean sandstone. The offset of the fault is not visible (**a**) core sample with a white arrow showing the position from where the sample for laboratory analysis was taken. (**b**) Results from absolute gas and brine permeability measurements from the host and fault-rock under different stresses. Note the stress-related permeability reduction. (**c**) BSEM image from host rock (**d**) BSEM image from fault rock; note the PFFR border (green arrow).

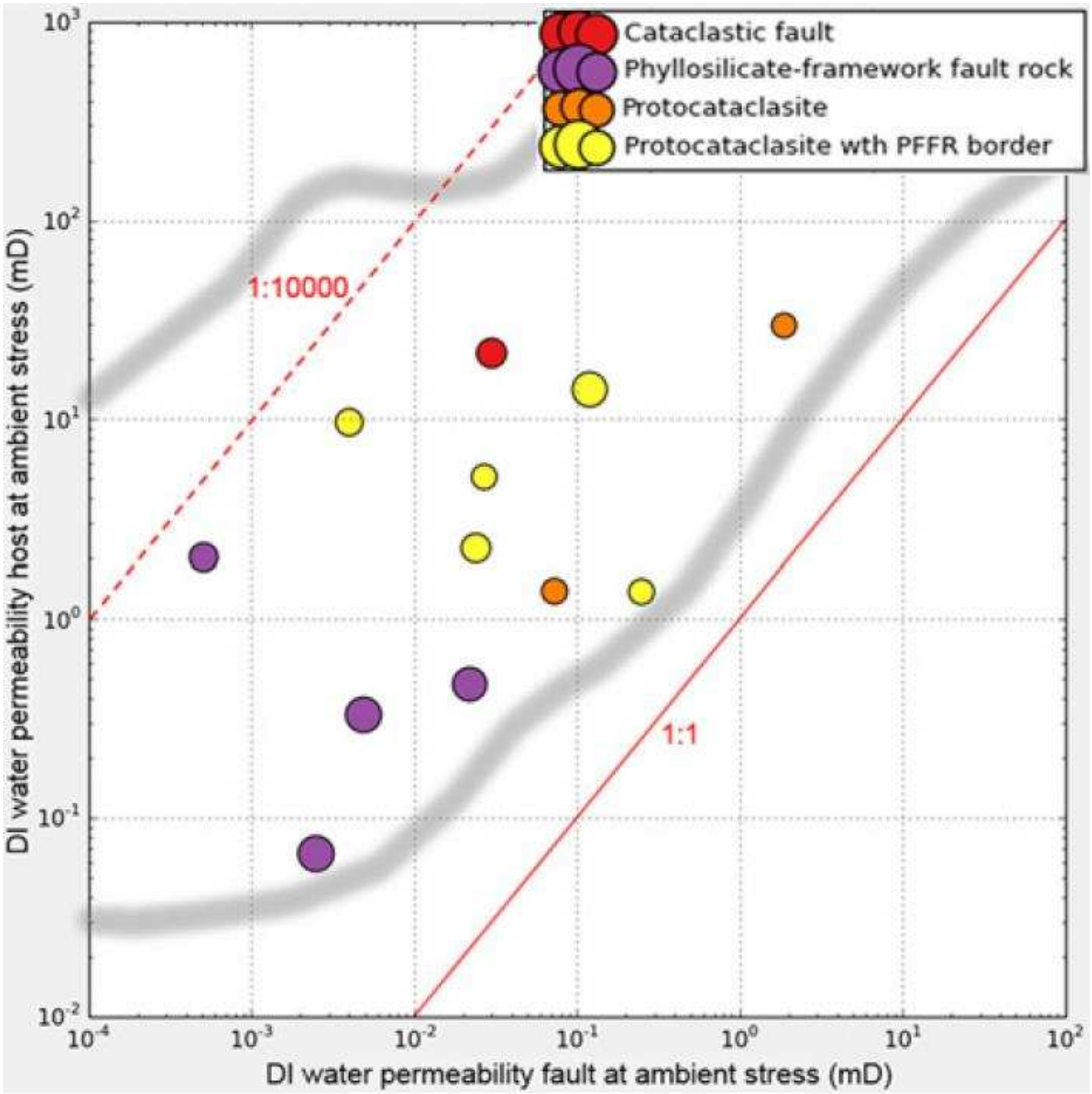

Fig. 11. Host rock versus fault rock absolute permeability measured under ambient stress and with deionized water as reservoir fluid. The dots represent the field data. The grey outlines represent the ranges of data from an in-house database. The point size correlates with the Vclay content of the fault rocks.

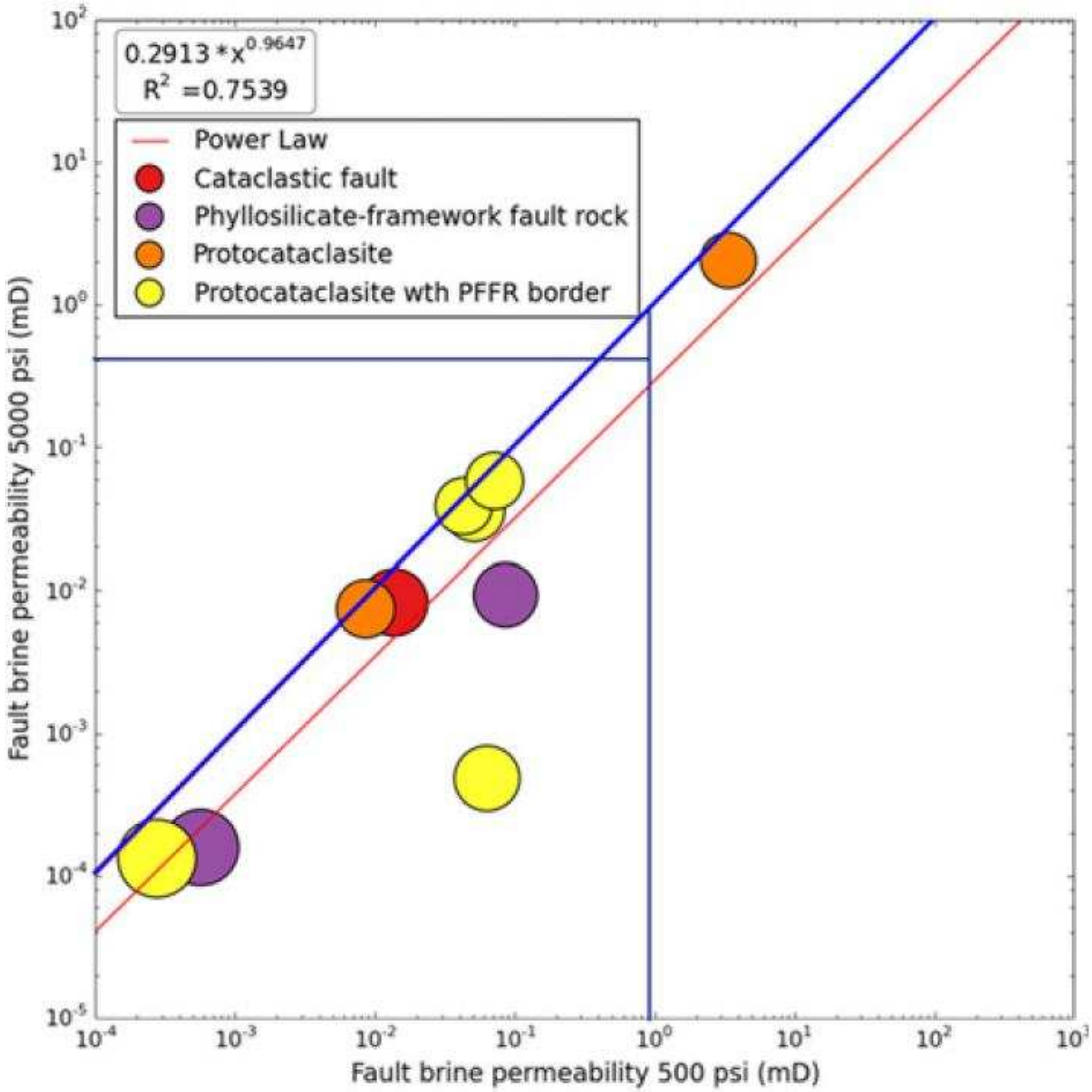

Fig. 12. Fault rock brine permeabilities from the field data under 500psi versus 5000psi. The point size correlates to the fault rock Vclay content. Blue line = 1:1 relation, red line = power law regression.

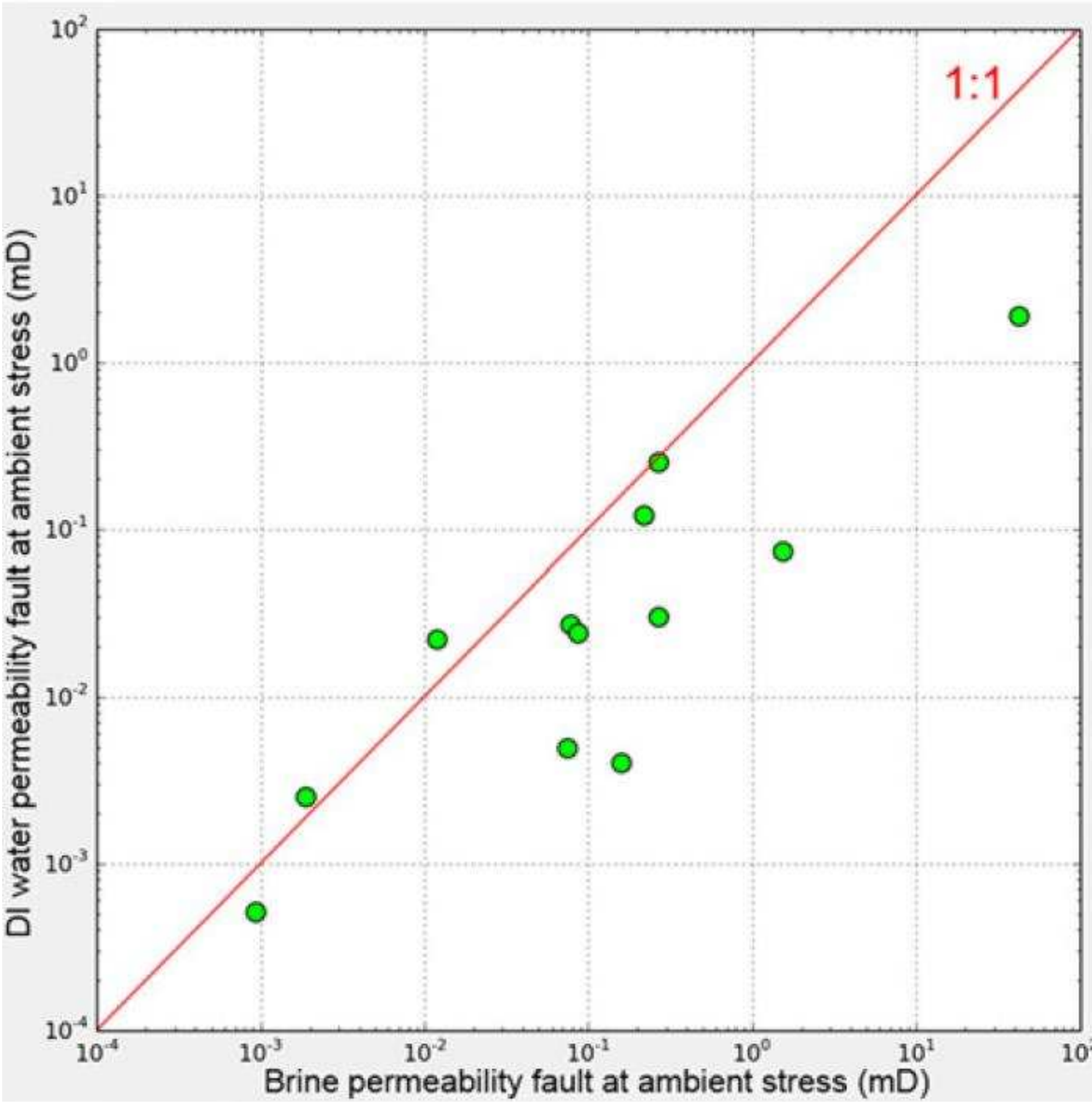

Fig. 13. Fault rock permeabilities from field data measured under ambient stress using a 30% salinity brine and deionized water as a reservoir fluid.

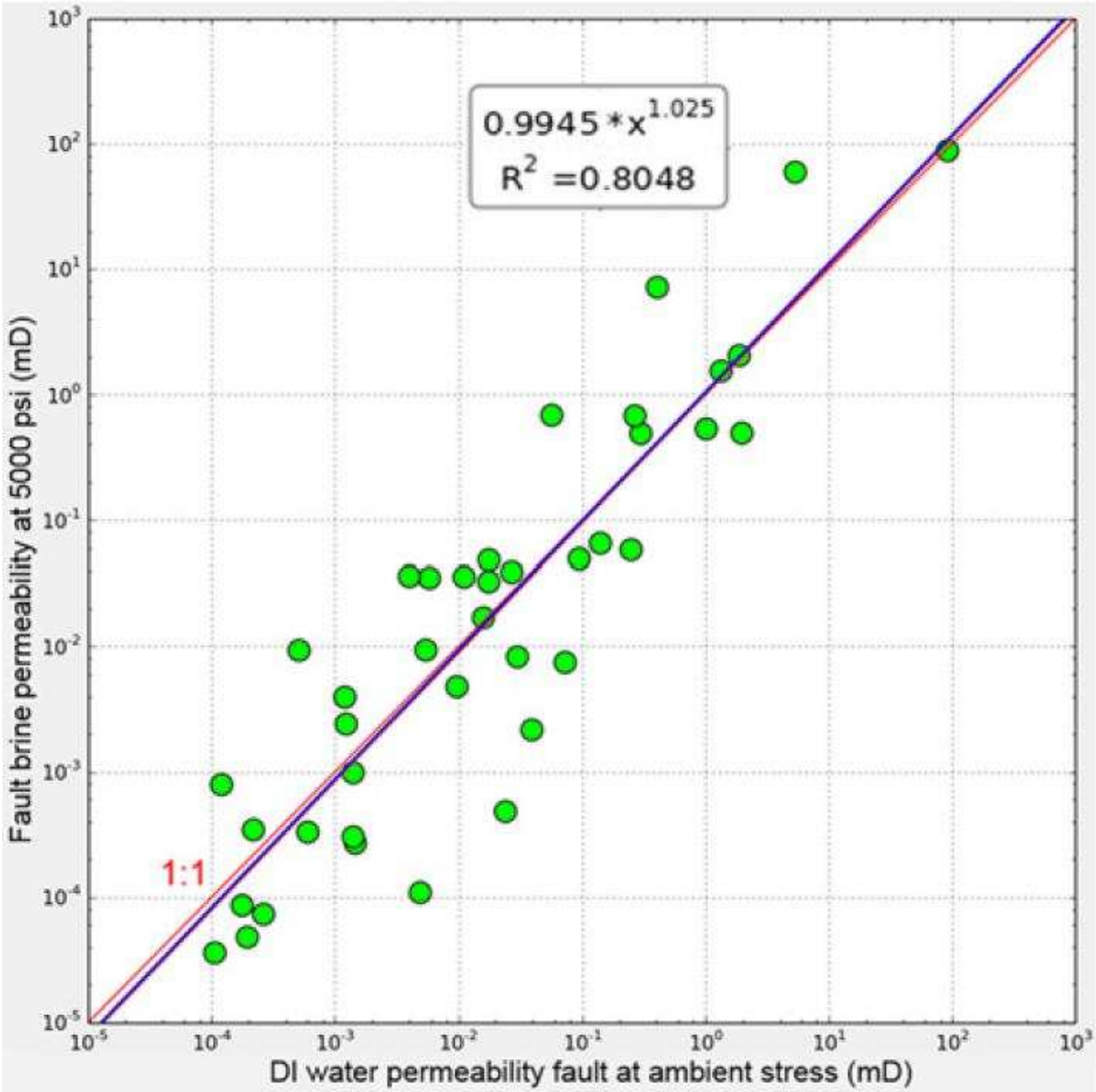

Fig. 14. Fault rock absolute permeabilities from a larger dataset measured under 5000psi stress with formation compatible brine versus data measured at ambient stress and deionized water as reservoir fluid. These fault rocks are similar to those analysed during the current study. The observation that the regression (blue) is almost the same as the1:1 relationship (red) between the two measurement techniques suggests that it is reasonably safe to use the data collected at low stress with distilled water as an analogue for measurements conducted at in situ stresses using formation compatible brine.

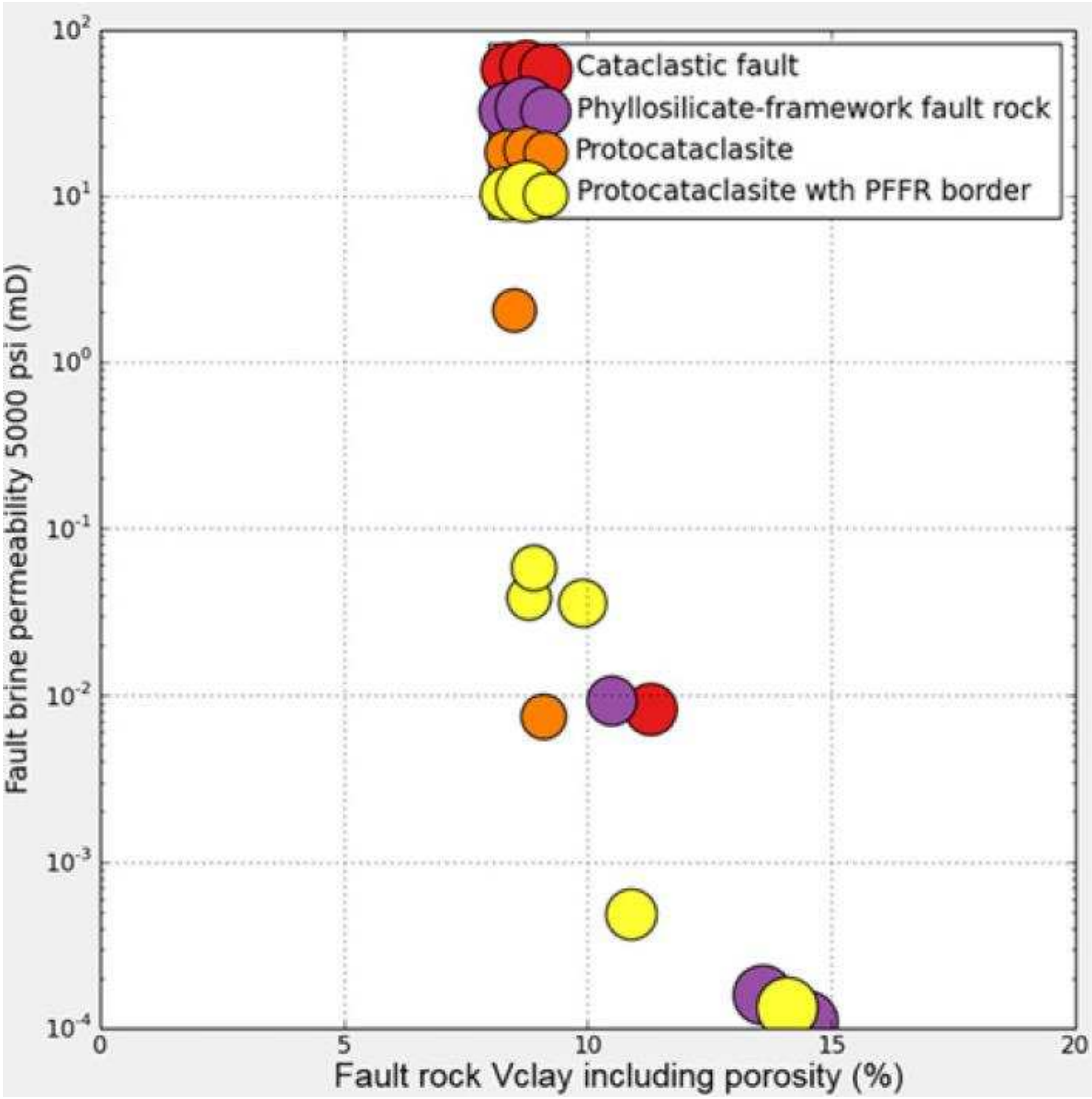

Fig. 15. Fault rock brine permeability under 5000psi stress plotted against the fault rock clay content.

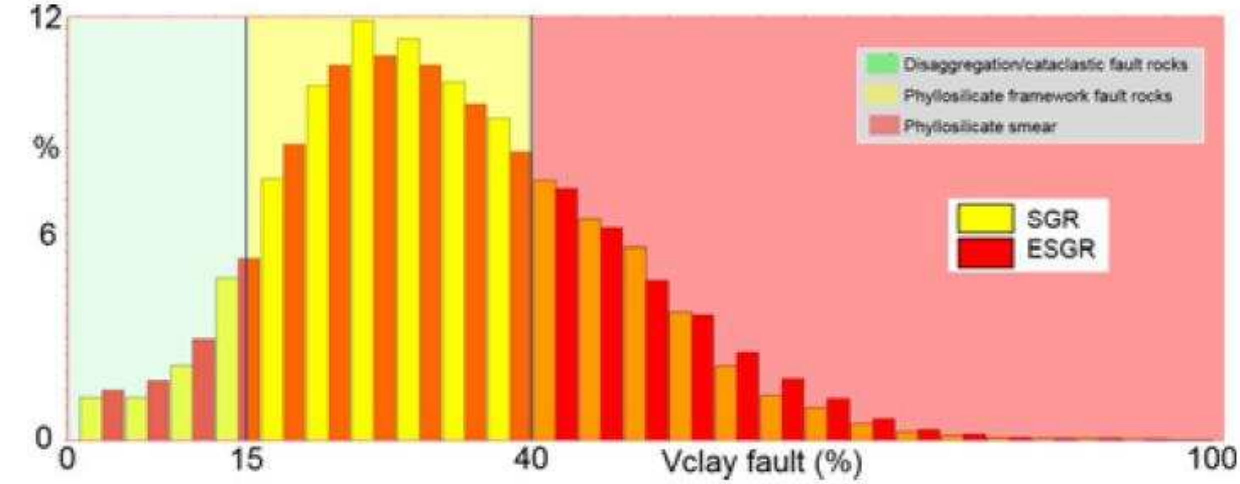

Fig. 16. Histogram plot of fault rock Vclay content for the reservoir scale faults based on a base case Vclay geomodel and a base case fault throw. The difference applying the SGR (Yielding, 2002) and ESGR (Freeman *et al.,* 2010) algorithm as a fault rock Vclay predictor is shown. The ESGR is for a hangingwall and footwall combination with a weighting factor of 0.15.

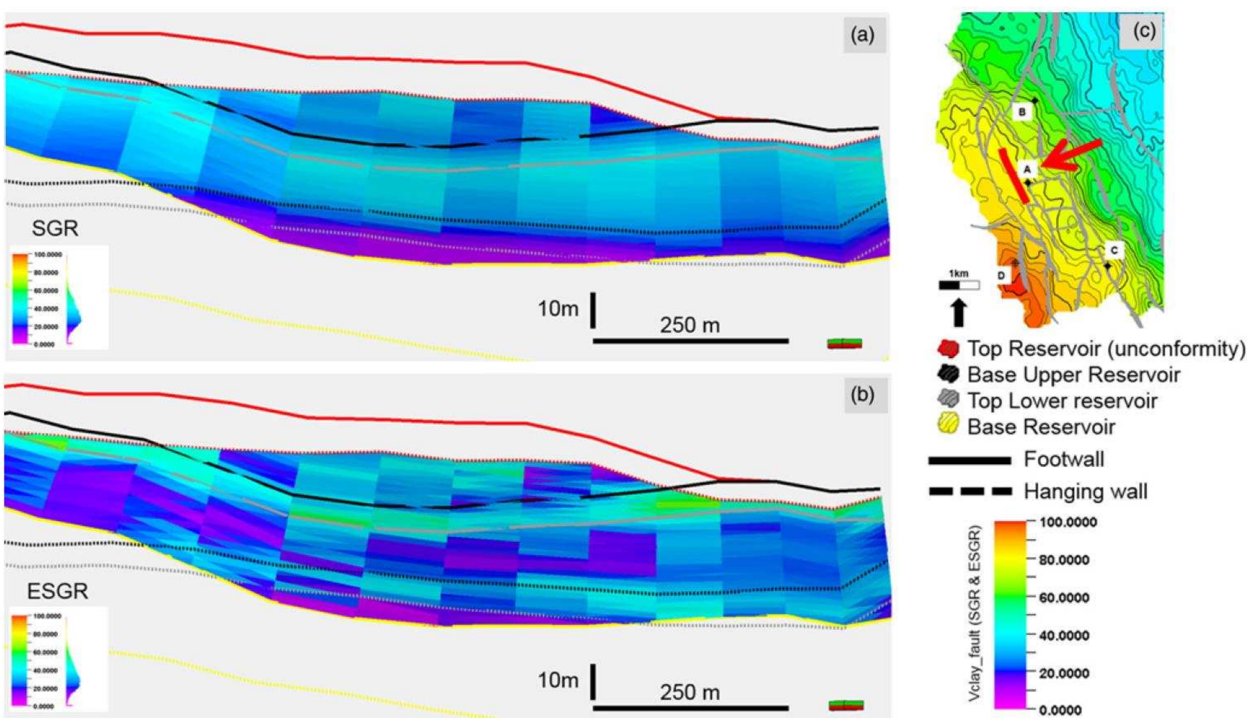

Fig. 17. Calculated fault rock Vclay content applying two different fault rock Vclay prediction algorithms (**a**) SGR (**b**) ESGR. (**c**) Near top reservoir map with seismic scale faults. The area colour coded with fault properties on 'a' and 'b'corresponds to the reservoir-reservoir self-

juxtaposition. Note that the reservoir is divided further into an upper and lower interval with a more silty layer in-between (see also Fig. 6); between the black and grey horizon. The view is towards the SW onto the fault plane.

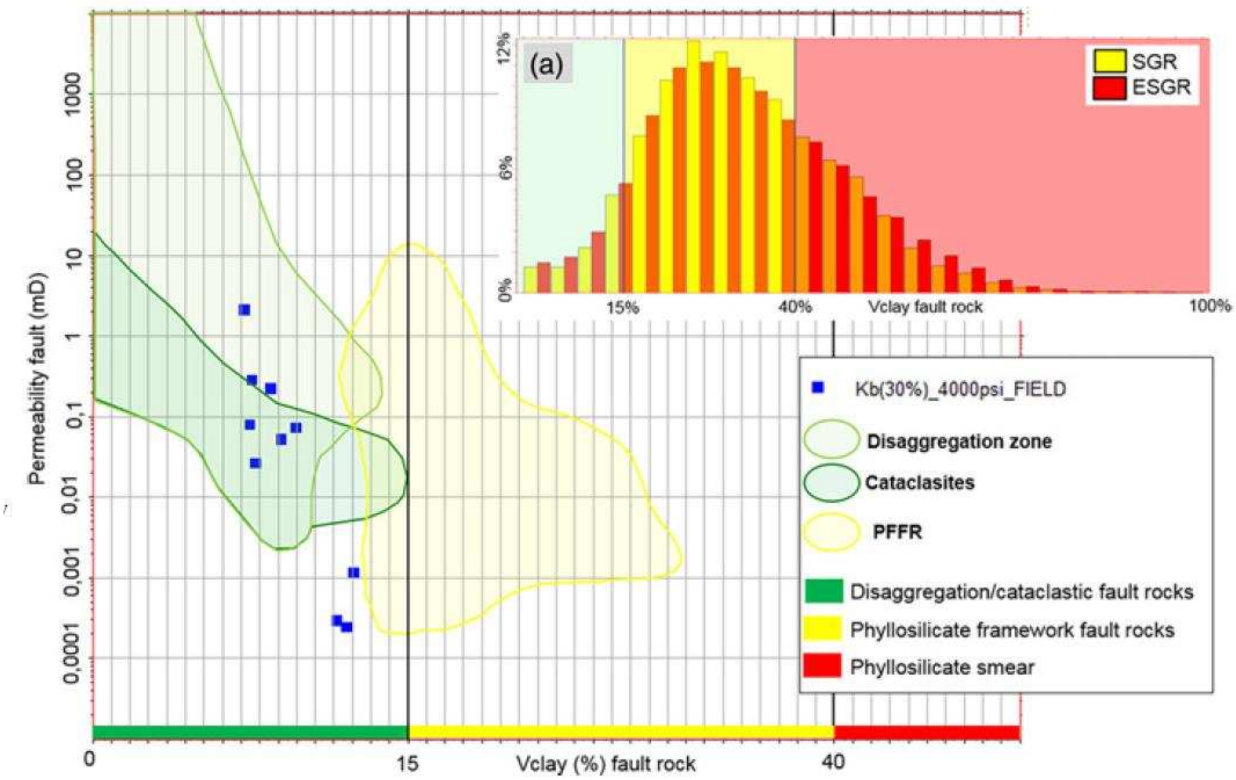

Fig. 18. Fault rock permeability versus Vclay from field data (blue squares), measured under 4000psi with 30% salinity brine and data from an in-house database (shaded areas) measured under 70psi and with deionized water as reservoir fluid. Fault rock samples in the in-house database are from reservoirs from the same area, the same time and underwent a similar tectonic history. (**a**) Histogram of fault rock Vclay content distribution for the reservoir scale faults. Green background = cataclasites/ disaggregation zones, yellow background = phyllosilicate framework fault rocks (PFFR), red background = phyllosilicate smear.

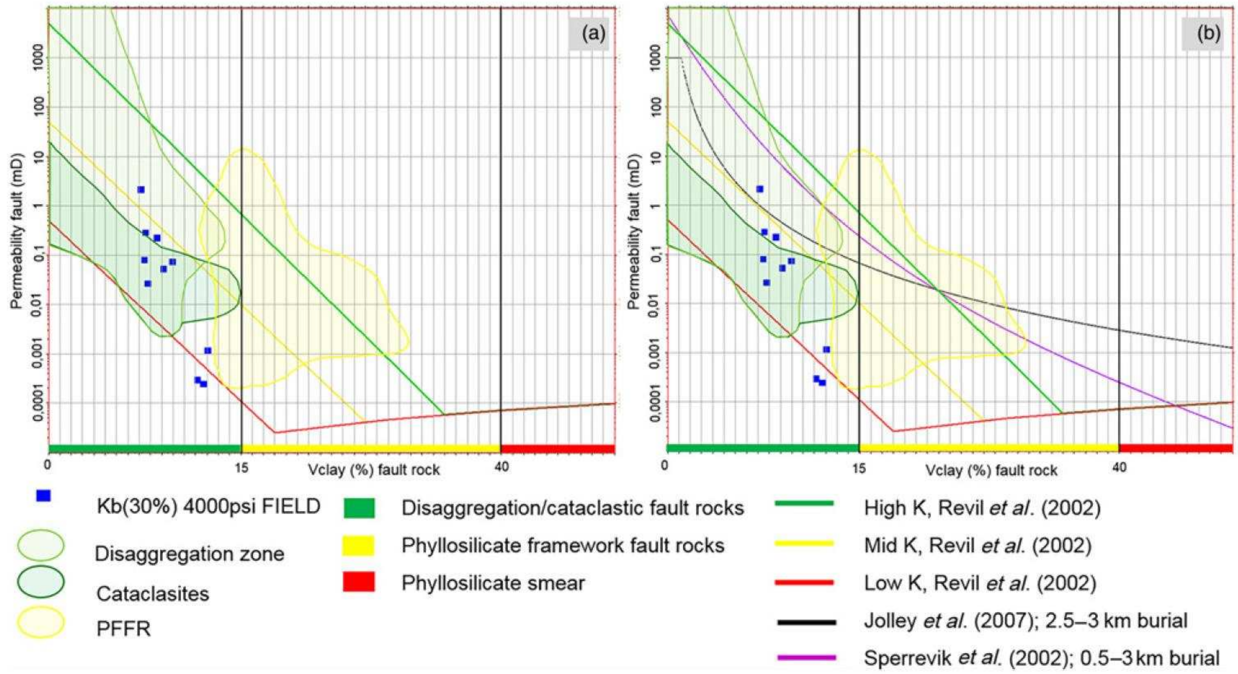

Fig. 19. Fault rock permeability versus Vclay from field data (blue squares), measured under 4000psi with 30% salinity brine and data from an in house database (shaded areas) measured under 70psi and with deionized water as reservoir fluid. The data are from burial depths between 2300m and 3100m, similar to the field data. (**a**) High, Mid and Low predictive functions for the seismic scale faults, using the algorithms from Revil *et al.* (2002). (**b**) including the fault rock permeability prediction curves based on the algorithms from Sperrevik *et al.* (2002) and Jolley *et al.* (2007).

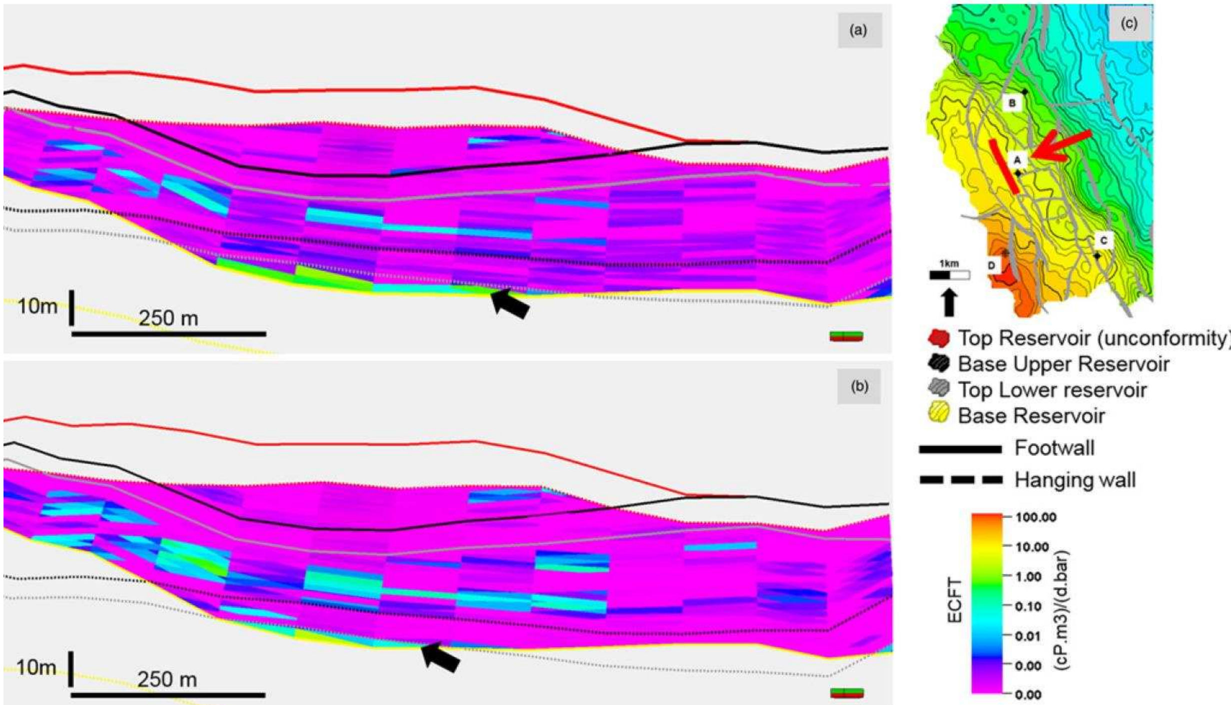

Fig. 20. Effect of increase in fault throw on ECFT (Freeman *et al*., 20010). (**a**) base case throw. (**b**) 20% increase of fault throw. Note the reduction of the area with high ECFT (black arrow) where the lower reservoir is self-juxtaposed. See discussion in text.

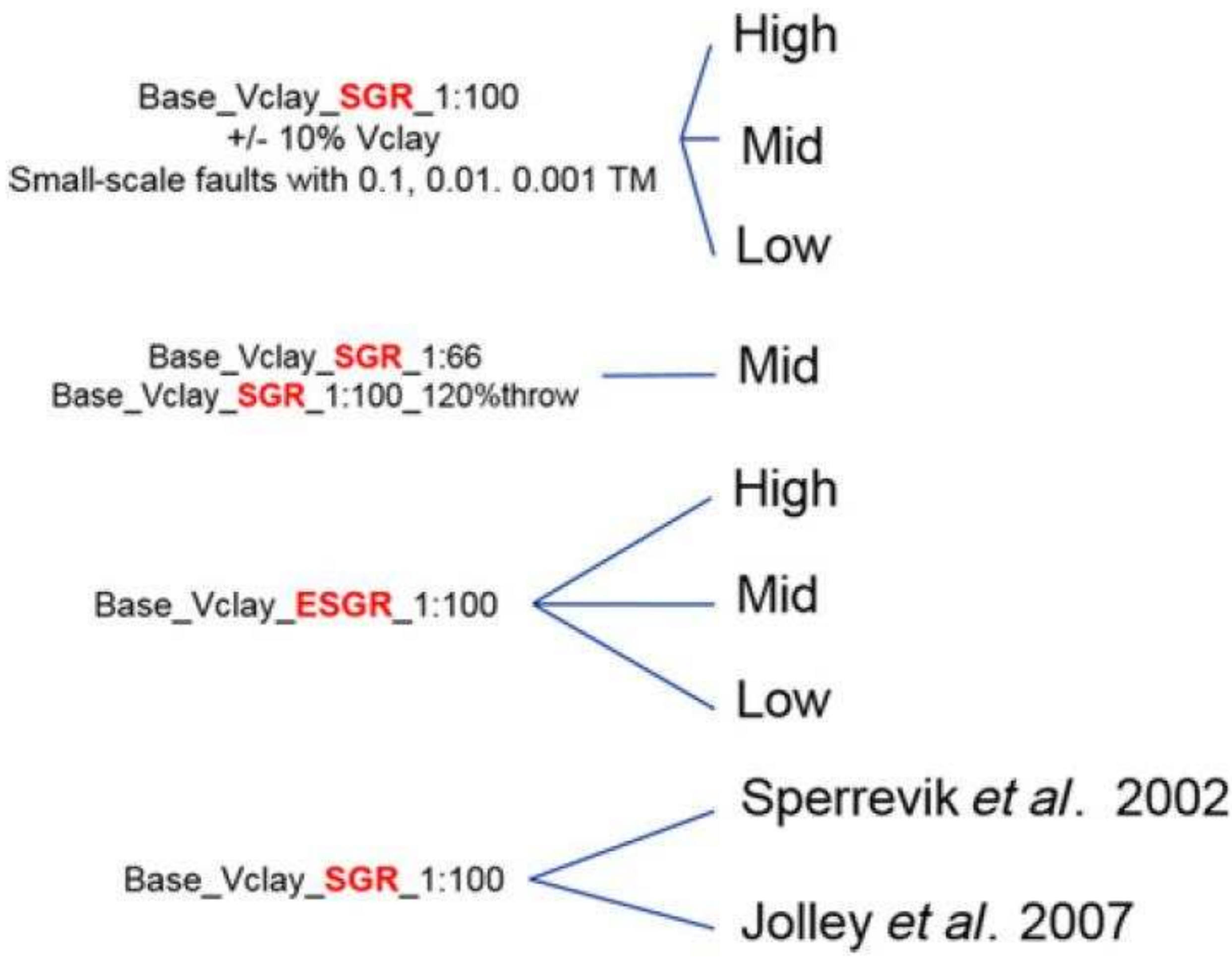

Fig. 21. Summary of the scenario for fault rock properties that were run in the dynamic simulation model. The "High", "Mid" and "Low" cases correspond to the three scenarios for high, mid and low permeability vs. clay content curves, based on the algorithms from Revil *et al.* (2002).

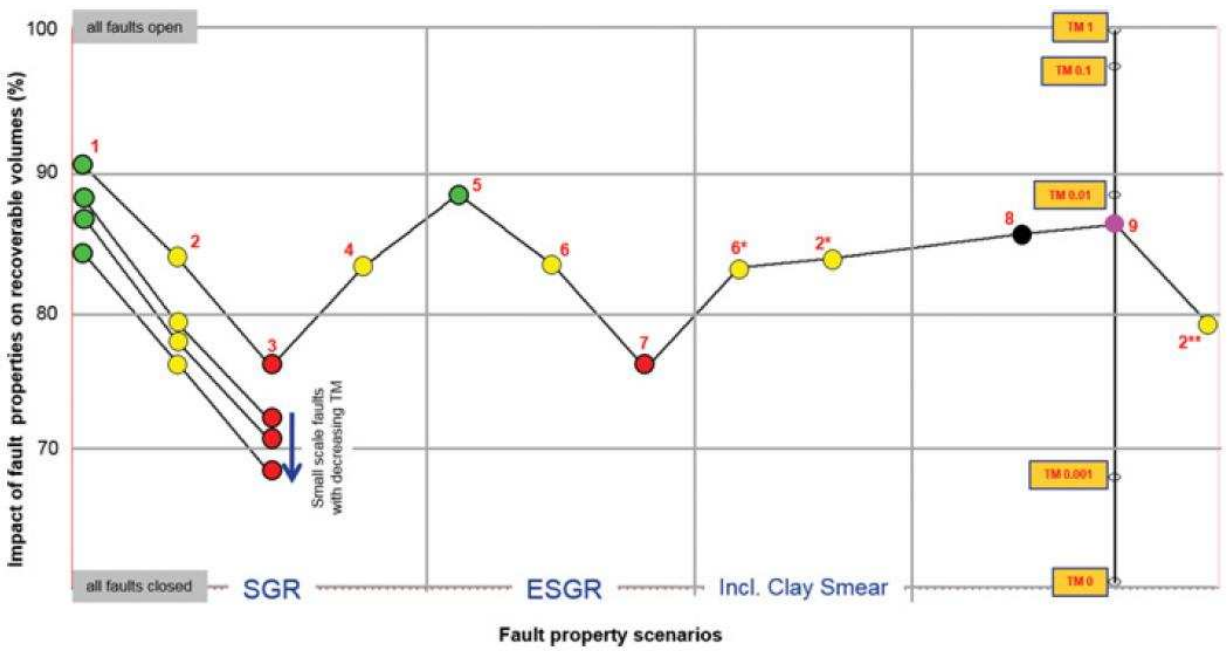

Fig. 22. Imapct of different fault properties scenarios on recoverable volumes, thickness to throw ratio of 1:100, except case 4 with 1:60; 1&5)High_K, 2&6) Mid_K, 3&7) Low_K, 4) Mid_K with thickness to throw ratio of 1:66, 6* & 2*) same as case 2 and 6, but taking into account the potential of clay smear in addition to the fault gouge, 8) Jolley et al.,2007, 9) Sperrevik etal., 2002, 2**) Mid_K case 2 with 20% increase in throw. Note the impact of incorporating the small scale faults on the recoverable volume range. A bulk transmissibility multiplier of 0.1, 0.01 and 0.001 has been assigned to the small scale faults. Note that all cases, except 8 and 9 use the mixing algorithms from Revil *et al*. (2002) to calculate the fault rock permeabilities. The SGR is used as a fault rock Vclay prediction for 8 & 9. The Y-axis is dimensionless.

	Porosity (%)	Permeability (mD)
High	35	5000
Mid	28	50
Low	20	0.5
Clay		0.00028

Table 1. Input values for the High, Mid, Low fault rock permeability predictive functions. The porosities and permeabilities in the High, Mid and Low rows correspond to the sandstones. Note

that these are host rock parameters, which are used in the mixing model proposed by Revil *et al.* (2002).